Chapter 1

Crystalline Inorganic Solid Electrolytes Computer Simulations and Comparisons with Experiment

M. D. Johannes[1] and N. A. W. Holzwarth[2]

[1] *Materials Science and Technology Division, U.S. Naval Research Laboratory, Washington, D. C., USA*

[2] *Department of Physics, Wake Forest University, Winston-Salem, N. C., USA*

This chapter presents examples of the use of first principles computer simulations in the study of two families of solid electrolyte materials – namely the family of Li phosphate, phospho-nitride, and thiophosphate materials and the family of Li oxide garnet materials. The simulation work together with related experimental studies of these solid electrolytes supports the continued development of all-solid-state battery technology.

1. Introduction and Overview

The use of crystalline solids as electrolytes in battery applications has a long history as discussed in several review articles and monographs.[1,2] The purpose of this chapter is to describe examples of the use of first-principles calculations in the development of two families of solid electrolyte materials – namely Li phosphates and thiophosphates (Section 2) and Li oxide garnets (Section 3). Beyond the scope of this chapter, there have been quite a few successful first-principles studies of other electrolytes. For example, the recent experimental discovery of $Li_{10}GeP_2S_{12}$ as a superionic conductor by Kamaya *et al.*[3] has generated significant experimental and theoretical work including a study of the phase and electrochemical stability and Li^+ conductivity by Ong *et al.*[4]

1.1. *Computational methods*

The computations discussed in this work are based on so-called "first-principles" electronic structure methods. The term "first-principles" implies a series of well-developed approximations to the exact quantum-mechanical description of a material with N_e electrons and N_N nuclei. Denoting the electron coordinates by $\{\mathbf{r}_i\}$ $(i = 1, 2, \ldots N_e)$ and nuclear coordinates by $\{\mathbf{R}_a\}$ $(a = 1, 2, \ldots N_N)$, the many-particle Schrödinger equation takes the form

$$\mathcal{H}\left(\{\mathbf{r}_i\}, \{\mathbf{R}_a\}\right) \Psi_\alpha\left(\{\mathbf{r}_i\}, \{\mathbf{R}_a\}\right) = E_\alpha \Psi_\alpha\left(\{\mathbf{r}_i\}, \{\mathbf{R}_a\}\right), \tag{1}$$

where $\mathcal{H}$ denotes the quantum mechanical Hamiltonian, E_α and $\Psi_\alpha\left(\{\mathbf{r}_i\},\{\mathbf{R}_a\}\right)$ denote the energy eigenvalue and the corresponding eigenfunction, respectively. The solution of Eq. (1) with $N_N N_e$ coupled variables, is intractable for all but the smallest systems. The analysis of Born and Oppenheimer,[5] noting that the electron mass is 10^{-3} times smaller than the nuclear mass, leads to an approximate separation of the nuclear and electronic motions. Operationally, the nuclei are treated as classical particles with interaction energies consistently determined by expectation values of the electronic Hamiltonian. The electronic Hamiltonian and the corresponding Schrödinger equation should be solved for each set of nuclear positions $\{\mathbf{R}_a\}$. The solution of the Born-Oppenheimer electronic Schrödinger equation is further approximated with the use of density functional theory developed by Kohn, Hohenberg, and Sham,[6,7] treating the N_e electrons in a self-consistent mean-field due to both the electrons and nuclei. The reliability of density functional theory in the representation of real materials depends on the development of the exchange-correlation functional form. While this remains an active area of research, the local density approximation (LDA)[8] and the generalized gradient approximation (GGA)[9] often work well, particularly for modeling the ground state properties of solid electrolytes. In density functional theory, the electronic energy of a system of N_e electrons can be expressed as a sum of contributions:

$$E(\rho,\{\mathbf{R}_a\}) = E_K + E_{ee} + E_{xc} + E_{eN} + E_{NN}, \tag{2}$$

representing the electronic kinetic energy, the coulombic electron-electron repulsion, the exchange-correlation energy, the electron-nuclear interaction energy, and the nuclear-nuclear interaction energies respectively. The electron density $\rho(\mathbf{r})$ is self-consistently determined from Kohn-Sham single particle wavefunctions for each state n:

$$H^{KS}\psi_n = \epsilon_n\psi_n \quad \text{where} \quad \rho(\mathbf{r}) = \sum_{n=1}^{N_e} |\psi_n(\mathbf{r})|^2 \tag{3}$$

at self-consistency. The Kohn-Sham Hamiltonian is determined from the functional derivative

$$H^{KS} = \frac{\partial E(\rho,\{\mathbf{R}_a\})}{\partial\rho(\mathbf{r})}. \tag{4}$$

In addition to well-controlled mathematical and physical approximations, numerical approximations are needed to solve the density functional equations. There are many successful numerical schemes many of which grew from the frozen-core approximation[10] and the refinement of the pseudopotential formalism[11] with the development of first-principles pseudopotentials.[12,13] A significant boost to the field was contributed by Car and Parrinello[14] who showed that within the Born-Oppenheimer approximation, the self-consistent electronic structure algorithm could be efficiently coupled to the adjustment of the nuclear coordinates for structural and molecular

dynamics studies. In addition to the adjustment of the nuclear coordinates, techniques were developed to allow for variable simulation cells in order to simulate the effects of pressure, stress, or phase transitions.[15–17] Response function methods and density-functional perturbation theory methods were developed by Gonze,[18,19] allowing for the exploration of materials properties in the vicinity of equilibrium including the dynamical matrix and phonon modes. The efficiency and accuracy of the pseudopotential approach was significantly improved with the introduction of so-called ultra-soft pseudopotentials (USPP) by Vanderbilt[20] and the projector augmented plane wave (PAW) method by Blöchl.[21]

An invaluable contribution to the success of computational studies of materials, particularly those discussed in this chapter, has been the development of several open source software projects such as ABINIT[22] and QUANTUM ESPRESSO.[23] These codes make use of many of the state-of-the-art formalism developments including those listed above. These projects promote scientific productivity by reducing the duplication of coding efforts and by allow developers and users to share in the implementation and debugging of a common code system. For the simulations in Sec. 2, the pseudopotential data files were generated using the ATOMPAW package[24] and the USPP package[20] For the simulations in Sec. 3, the Vienna Ab Initio Software Package (VASP) was used.[25,26] Also important is the development of visualization tools. For this work, OpenDx,[27] XCrySDen,[28,29] and VESTA[30] were used.

For solid electrolytes which are electronically insulating and which operate in their ground electronic states, the calculation of the electronic energy $E(\rho, \{\mathbf{R}_a\})$ using density functional theory (Eq. (2)) works quite well. By using constrained optimization of the energy $E(\rho, \{\mathbf{R}_a\})$ over the nuclear coordinates $\{\mathbf{R}_a\}$, it is possible to study structural parameters of stable and meta-stable structures. A reasonable estimate of the heat of formation ΔH of each compound material can be computed from the ground state energies at zero temperature

$$\Delta H \approx E(\rho, \{\mathbf{R}_a\}) - \sum_e \nu_e E_e(\rho, \{\mathbf{R}_a\}), \tag{5}$$

where $E(\rho, \{\mathbf{R}_a\})$ denotes the computed electronic energy of the material per formula unit, ν_e denotes the number of atoms of element "e" in the formula unit, and $E_e(\rho, \{\mathbf{R}_a\})$ denotes the energy per atom in its standard state of the element as defined in the CRC Handbook[31] or the NIST JANAF Thermochemical Tables.[32] In practice, the calculation of $E(\rho, \{\mathbf{R}_a\})$ is subject to an arbitrary reference energy which depends on on the details of the code and of the pseudopotential datasets. If the electronic energy calculations for E and E_e are evaluated consistently with accurate convergence criteria, the ambiguity of the total energy disappears from the evaluation of Eq. (5). These measured and computed heats of formation are useful in quantifying the expected stability of the materials in various structures and compositions.

The first-principles approach can be extended to simulate ion mobilities. For

example, the "nudged elastic band"[33–35] method (NEB) can be used to estimate the migration energy E_m. The basic assumptions of this approach[34] are that the ion diffusion is slow enough so that the process is well described by Boltzmann statistics and that the diffusion rate is controlled by ion trajectories which pass through harmonic regions of the potential energy surface near minima and saddle points which represent transition states of the system. The computational effort is thus focused on finding the saddle points of the potential energy surfaces between local minimum energy configurations. Each of the diffusion paths considered is approximated by a series of transitions between pairs of local minima corresponding to meta-stable configurations. The search for the saddle point is implemented by assuming several intermediate "images" between each pair of local minima. Each of the images is relaxed until the forces perpendicular to the minimum energy path are less than the prescribed tolerance level. The energies between each pair of local minima is determined by interpolating between the energies of the images and E_m is determined from the difference between the highest and lowest energy along the path. The migration energy is related to the temperature dependent ionic conductivity $\sigma(T)$ with an Arrhenius relation[36,37]

$$\sigma(T) = \frac{K}{T} \mathrm{e}^{-E_A/kT}, \tag{6}$$

where the prefactor K depends on the material and k denotes the Boltzmann constant. In the case of a material with few intrinsic defects, the activation energy includes both the ion migration energy E_m and also the "formation" energy E_f associated with the creation of a defect. The usual case is that E_f is the energy to create a vacancy-interstitial pair and the activation energy is given by

$$E_A = E_m + \frac{1}{2} E_f. \tag{7}$$

This method was used to analyze the Li ion conductivity in Sec. 2.3.

In addition, the dynamics of Li ion diffusion subject to temperature were carried out using molecular dynamics (MD) simulations with the energies and forces derived from first principles (VASP) calculations at each time step. The results from MD simulations provide a convenient comparison to the NEB calculations from a more integrated, statistical point of view. While NEB calculations specifically evaluate the activation barrier by calculating the energy curve along a real-space trajectory, MD simulations are statistical and the activation barrier extracted is an "effective" barrier - essentially the average barrier experienced by the movement of all Li ions in the simulation. The mean squared displacement of the Li ions $< x^2 >$ is measured as a function of time and the diffusion constant, D can be extracted via the following:

$$D = \frac{1}{6} \frac{d(< x^2 >)}{dt} \tag{8}$$

where the factor of 6 comes from the three-dimensionality of the diffusion path. This analysis was used in Sec. 3.5.

Because diffusivity is activated, performing MD evaluations of $< x^2 >$ at various temperatures and fitting to an Arrhenius plot will yield an activation barrier of the form

$$D = D_0 \mathrm{e}^{-E_A/kT}, \tag{9}$$

A comparison of E_A derived in this manner from MD to NEB results can provide an estimate of E_f and also can reveal whether there is a single or perhaps many different Li ion paths accessed during diffusion. In principle, one advantage of the MD approach is that the prefactor D_0 is also determined, while the corresponding prefactor K of Eq. 6 is not computed in the NEB approach.

1.2. *Validation*

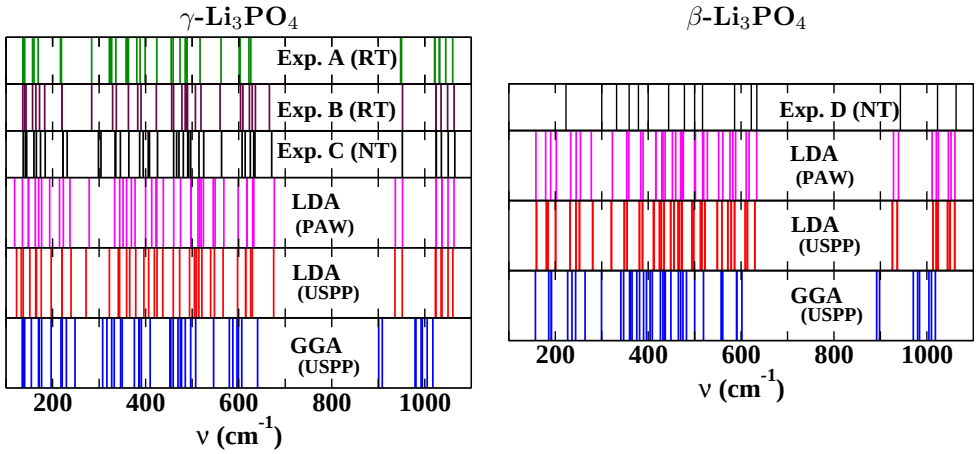

Fig. 1. Comparison of experimental and calculated Raman spectra for γ-Li_3PO_4 (left) and β-Li_3PO_4 (right). The experimental measurements were performed at room temperature (RT) and at liquid nitrogen temperature (NT). Exp. A was taken from Ref. [38] and Exp. B and C were taken from Ref. [39], and Exp. D was taken from Ref. [40]. These are compared with calculated results using PAW and USPP formalisms and LDA and GGA exchange-correlation functionals.

It is always important to ask the question: How reliable are computer simulations in describing real materials. Typically, it has been reported[41] that results obtained using the LDA exchange-correlation functional[8] tend to underestimate the lattice parameters by 2% while results obtained using the GGA exchange-correlation functional[9] tend to overestimate the lattice parameters by 1%. On the other hand, for most materials, the fractional coordinates computed for the non-trivial site positions are nearly identical (within 0.1%) for LDA and GGA calculations in comparison with experiment. Similar findings have been reported in the literature for a wide variety of computational studies of insulating, non-transition metal materials.

One quantitative indication of the accuracy of the calculations is the comparison of computed and measured lattice vibration modes. Fortunately, there have been

several reports of experimental measurements of Raman and infrared absorption spectra of crystalline Li_3PO_4;[38–40,42–44] therefore our simulations of the zone center phonon modes serve as a validity check the calculations. Figure 1 shows the spectra of Raman active modes calculated using the LDA and GGA exchange-correlation functions and USPP[20] and PAW[24] pseudopotential datasets compared with various experimental measurements for the γ and β structures. There is variation among the various experimental measurements for γ-Li_3PO_4, some of which can be attributed to temperature and some attributed to resolution. In terms of comparing experiment to the calculations, it is striking that for frequencies $\nu > 600$ cm^{-1}, the results calculated using the LDA functional are in good agreement with experiment, while the agreement deteriorates at lower frequencies. These high frequency modes are mainly due to internal vibrations of the PO_4 tetrahedra. The lack of agreement for the lower frequency modes is likely to be due to numerical error which is reflected in the differences between the two LDA calculations using USPP and PAW datasets. The good agreement between the simulations and experiment for the higher frequency vibrational modes of these materials motivated the choice of the LDA functional for most the simulation studies on the Li phosphates and thiophosphates covered in this review (Sec. 2).[41,45–53] On the other hand, for the simulations of garnet oxide materials discussed in Sec. 3 of this review, a sensitivity to more accurate lattice parameters motivated the choice of the GGA functional.[54]

2. Li phosphate, phospho-nitride, and thiophosphate crystalline electrolytes

The thin film solid electrolyte LiPON developed at Oak Ridge National Laboratory (ORNL),[55–63] is a very widely used solid electrolyte for thin film batteries and a number of other related technologies.[64] In addition to studies at ORNL, there has been considerable research[65–68] on the preparation and properties of LiPON materials. One of the outstanding attributes of LiPON electrolytes is its long term stability in contact with a pure lithium anodes.[69] By contrast, several other electrolyte candidates, such as for example lithium silicates and lithium silicate/phosphate composites, have been found[63] to react with lithium anode films. LiPON electrolytes have the composition of $Li_xPO_yN_z$. The LiPON electolytes with the highest ionic conductivities (10^{-6} S/cm) have a glassy structure and a range of values of $0.2 \leq z \leq 0.7$ representing the ideal nitrogen contribution.[55,65,70] At the present time, we know of no experimental evidence that crystalline members of the LiPON family of materials can approach the conductivities of the LiPON glasses, however, a systematic study of the LiPON family of crystalline materials[49] has proven useful for developing an understanding of the fundamental structures and properties of LiPON electrolytes. Meanwhile, the structurally and chemically related Li thiophosphate family of materials have recently received attention as promising candidates for solid-state electrolytes[71–81] where increased ionic conductivities as large as 10^{-3}

S/cm have been reported. These materials are characterized by the composition Li_vPS_w. The comparison between the crystalline Li phosphates and corresponding thiophosphates has provided further insight into solid electrolyte development.

Subsection 2.1 presents the energetics of lithium phosphates, lithium phosphonitrides, and lithium thiophosphates and related compounds. In order to facilitate comparisons between materials and comparisons of calculations with experiment, the material energies are expressed in terms of the heats of formation. Subsection 2.2 details the structural forms such as phosphate and thiophosphate monomers, dimers, and chains found from experiment and computation in view of their relative stabilities. Subsection 2.3 reviews the calculated and experimental Li ion conduction properties of these materials.

2.1. *Heats of Formation*

The estimation of the heat of formation ΔH as given in Eq. (5) has been been carried out for a large number of Li phosphate, Li phospho-nitride, and Li thiophosphate crystals as listed in Table 1. For these materials, the elemental reference states are given as follows. Li is referenced to solid Li in its body-centered cubic structure which is modeled directly. P is referenced to its "white" structural form. Since this structure is difficult to model directly, the calculations first simulated the structure of "black" phosphorus in its orthorhombic structure (*Cmce* (#64))[82] and the white P reference energy was determined by adding the experimental value[31] of the heat of formation for white P relative to black P of 39.3 kJ/mol. S is referenced to its orthorhombic structure (α-S_8 – *Fddd* (#70))[83] which is modeled directly. O and N are referenced to their gaseous molecular forms. For these, additional steps had to be taken because, while the Kohn-Sham formalism using the LDA exchange-correlation functional is known to do an excellent job of comparing the energies of materials in the solid state, molecular energies are treated less well. Accordingly, an approach similar to that of Wang *et al.*[84] was used. That is, a least squares fit to standard heats of formation for N and O containing compounds having enthalpy data as indicated with "*" in Table 1 was used to set the reference energies of O and N.

While all calculations are based on results for idealized crystals corresponding to experimental temperatures of 0 K, we estimate that the additional heat and work needed to bring the materials to the standard temperature of 298.15 K is negligible compared to the overall error of the calculational methods. The results of our calculations of the total energies of all of the materials of this study, including the materials used in the fit are given in Table 1. The calculated results agree with the available experimental results within 0.5 eV. Similar tables have been reported in earlier work;[47,49,51,53] small differences in the calculated values of ΔH are indicative of variations in the computational details and in the accuracy of the experimental heats of formation used for the O and N standards. (In fact, the heats of formation quoted in Refs. [31] and [32] often lack specific structural information.)

Table 1. Calculated heats of formation for Li phosphates, phospho-nitrides, and thiophosphates and related materials. The structural designation uses the the notation defined in the International Table of Crystallography[85] based on structural information reported in the International Crystal Structure Database.[86] The heats of formation ΔH (eV/FU) are given in units of eV per formula unit. When available from Ref. [31] and [32] experiment values are indicated in parentheses. Those indicated with "*" were used fitting the O and N reference energies as explained in the text.

Material	Structure	ΔH (eV/FU)
β-Li_3PO_4	$Pmn2_1$ (#31)	-21.23
γ-Li_3PO_4	$Pnma$ (#62)	-21.20 (-21.72*)
γ-Li_3PS_4	$Pmn2_1$ (#31)	- 8.37
β-Li_3PS_4	$Pnma$ (#62)	- 8.28
$Li_4P_2O_6$	$P\bar{3}1m$ (#162)	-29.72
$Li_4P_2O_7$	$P\bar{1}$ (#2)	-33.97
$Li_5P_2O_6N$	$P\bar{1}$ (#2)	-33.18
$Li_4P_2S_6$	$P\bar{3}1m$ (#162)	-12.42
$Li_4P_2S_7$	$P\bar{1}$ (#2)	-11.59
$Li_7P_3O_{11}$	$P\bar{1}$ (#2)	-54.84
$Li_7P_3S_{11}$	$P\bar{1}$ (#2)	-20.01
$LiPO_3$	$P2/c$ (#13)	-12.75
$LiPN_2$	$I\bar{4}2d$ (#122)	- 3.65
$s1$-Li_2PO_2N	$Pbcm$ (#57)	-12.35
SD-Li_2PO_2N	$Cmc2_1$ (#36)	-12.47
SD-Li_2PS_2N	$Cmc2_1$ (#36)	- 5.80

Material	Structure	ΔH (eV/FU)
N_2O_5	$P6_3/mmc$ (#194)	- 0.94 (- 0.45*)
P_3N_5	$C2/c$ (#15)	- 3.02 (- 3.32*)
h-P_2O_5	$R3c$ (#161)	-15.45 (-15.53*)
o-P_2O_5	$Fdd2$ (#43)	-15.78
P_2S_5	$P\bar{1}$ (#2)	- 1.93
P_4S_3	$Pnma$ (#62)	- 2.45 (- 2.33)
SO_3	$Pna2_1$ (#33)	- 4.84 (- 4.71*)
Li_3N	$P6/mmm$ (#191)	- 1.60 (- 1.71*)
Li_2O	$Fm\bar{3}m$ (#225)	- 6.10 (- 6.20*)
Li_2O_2	$P6_3/mmc$ (#194)	- 6.35 (- 6.57*)
Li_3P	$P6_3/mmc$ (#194)	- 3.47
Li_2S	$Fm\bar{3}m$ (#225)	- 4.30 (- 4.57)
Li_2S_2	$P6_3/mmc$ (#194)	- 4.09
$LiNO_3$	$R\bar{3}c$ (#167)	- 5.37 (- 5.01*)
Li_2SO_4	$P2_1/c$ (#14)	-14.63 (-14.89*)

It is expected that relative energies between structurally and chemically similar materials are considerably more accurate than the overall error.

For each material listed in Table 1 the optimization calculations were initiated with indicated crystal structure. For most of the materials, the crystal structures were reported in the International Crystal Structure Database (ICSD)[86] and/or in original experimental references. However, as explained in subsection 2.2, a few of material structures listed in Table 1 are hypothetical in the sense that they have not (yet) been experimentally realized, although their idealized structures are readily accessible through computation. The results of Table 1 are useful for understanding the structural and compositional stabilities of these materials.

2.2. *Structural forms of crystalline electrolytes*

For the Li phosphate, phospho-nitride, and thiophosphate electrolytes of this study, Table 2 lists the lattice parameters corresponding to the structural optimization energies reported in Table 1. While the calculated lattice constants are typically 2% smaller than the experimental values, with a few exceptions, the calculated results for lattice shapes and internal parameters are in good agreement with experiment.

A striking property of the Li phosphate, phospho-nitride, and thiophosphate electrolytes is their structural similarities and their compositional patterns. For the

Table 2. Calculated and measured lattice constants (in $\mathring{A}$) and angles (in degrees) for Li phosphate, phospho-nitride, and thiophosphate crystals. When available, the experimental reference is listed in [ ] brackets.

	Calculation						**Experiment**					
Material	a	b	c	α	β	γ	a	b	c	α	β	γ
β-Li_3PO_4 [87]	5.99	5.13	4.74	90	90	90	6.23	5.23	4.86	90	90	90
γ-Li_3PS_4 [88]	7.57	6.43	6.06	90	90	90	7.71	6.54	6.14	90	90	90
γ-Li_3PO_4 [89]	10.28	6.00	4.82	90	90	90	10.49	6.12	6.93	90	90	90
β-Li_3PS_4 [88]	12.86	7.81	5.94	90	90	90	12.82	8.22	6.12	90	90	90
$Li_4P_2O_7$ [90]	8.36	6.98	5.11	112	90	104	8.56	7.11	5.19	111	90	103
$Li_5P_2O_6N$	8.43	7.16	4.83	110	90	101						
$Li_4P_2S_7$	10.67	8.80	5.79	111	90	91						
$Li_7P_3O_{11}$	9.54	4.97	10.39	103	116	72						
$Li_7P_3S_{11}$ [74]	12.01	6.15	12.23	102	114	72	12.50	6.03	12.53	103	113	74
$Li_4P_2O_6$	4.76	4.76	5.36	90	90	120						
$Li_4P_2S_6$ [91]	5.95	5.95	6.37	90	90	120	6.07	6.07	6.58	90	90	120
$LiPO_3$ [92]	12.92	5.27	16.19	90	99	90	13.07	5.41	16.45	90	99	90
$LiPN_2$ [93]	4.47	4.47	7.24	90	90	90	4.58	4.58	7.12	90	90	90
s_1-Li_2PO_2N	5.33	4.67	9.13	90	90	90						
SD-Li_2PO_2N [52]	8.87	5.30	4.65	90	90	90	9.07	5.40	4.69	90	90	90
SD-Li_2PS_2N	11.46	6.30	4.91	90	90	90						

LiPON materials, having the general composition $Li_xPO_yN_z$, the stoichiometry is generally restricted to the relation $x = 2y + 3z - 5$. This implies the formal ionic charges of Li^{+1}, O^{-2}, N^{-3}, and P^{+5} which is consistent with most of the existent LiPON materials. For the Li thiophosphate materials the general composition is Li_vPS_w. The restricted relationship consistent with the Li phosphates is $v = 2w - 5$ implying the formal ionic charges of Li^{+1}, S^{-2}, and P^{+5}. This relationship is followed by many of the Li thiophosphates with some interesting exceptions such as $Li_4P_2S_6$.

While a wide variety of structural forms have been reported, a useful categorization is monomer, dimer, and chain structures. These are discussed in more detail below.

2.2.1. *Monomer-structured materials*

The category of monomer structures includes Li_3PO_4 and Li_3PS_4 both of which have been observed in several structural forms, including the orthorhombic structures having space groups $Pmn2_1$ (#31) and $Pnma$ (#62). Following the naming conventions of the previous literature, β-Li_3PO_4 refers to the $Pmn2_1$ structure and γ-Li_3PO_4 refers to the $Pnma$ structure. By contrast for lithium thiophosphate, γ-Li_3PS_4 refers to the $Pmn2_1$ structure and β-Li_3PS_4 refers to the $Pnma$ structure.[88]

Calculations find the lowest energy structure for these materials to be the ones having the $Pmn2_1$ space group.[87,88] These structures are well-defined in the sense that the Wyckoff sites are fully occupied. While the lattice constants of β-Li_3PO_4 are approximately 80% of those of γ-Li_3PS_4, the fractional coordinates of the two

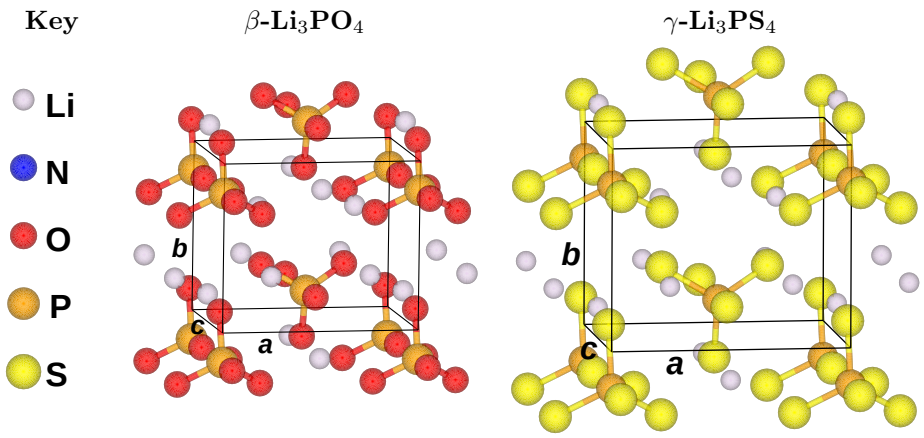

Fig. 2. Ball and stick diagram for the $Pmn2_1$ structures of β-Li_3PO_4 and γ-Li_3PS_4 (2 formula units per unit cell) from computational results. The key shown at the left indicates the ball convention used throughout Sec. 2.

materials are nearly identical. Figure 2 shows a ball and stick diagram of these two structures.

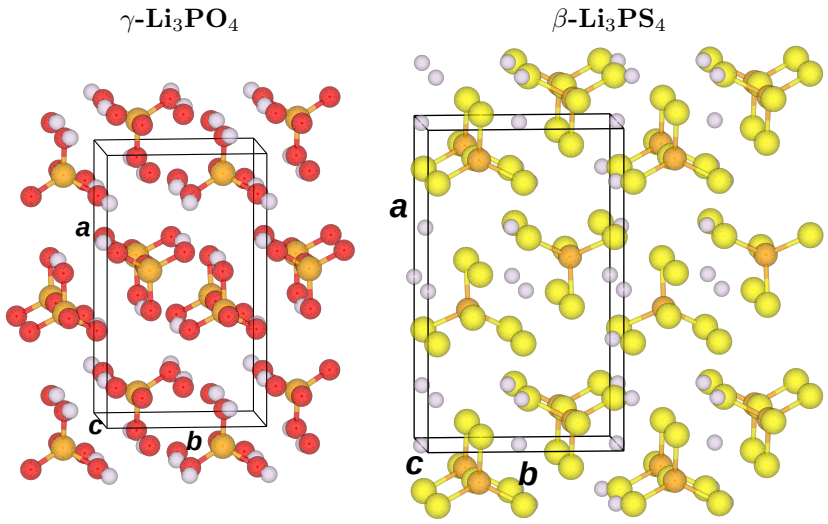

Fig. 3. Ball and stick diagram for the $Pnma$ structures of γ-Li_3PO_4 and β-Li_3PS_4 (4 formula units per unit cell) from idealized computational results.

The detailed structures of the $Pnma$ materials are more complicated than those of the $Pmn2_1$ materials. In γ-Li_3PO_4, shown in Fig. 3, the structure is described by full occupancy of the crystallographic sites.[89] A comparison with Fig. 2 shows that a crude approximation to the $Pnma$ structure can be derived from the $Pmn2_1$ structure by switching the a and b axes and then doubling the unit cell along

the a axis. Additional differences are due to the orientation of the phosphate or thiophosphate tetrahedra along the c-axis. For Li_3PS_4 in the $Pnma$ structure, further complication comes from the fact that experimental analysis of β-Li_3PS_4 finds that some of the Li sites are partially occupied[88,94] – namely the site labeled "b" in the Wyckoff notation is found to have an occupancy of 70% while the site labeled "c" is found to have an occupancy of 30%. In simulations of idealized perfect crystal structures, a structure with full occupancy of the "b" site was found to have the lowest energy. This is the structure reported in Tables 1 and 2 and shown in Fig. 3. The differences between the structures of γ-Li_3PO_4 and the idealized β-Li_3PS_4 structure shown in Fig. 3 are due primarily to the differences in the Li site positions.[53]

2.2.2. *Dimer-structured materials*

Li phosphate dimer structures have been found in the $P\bar{1}$ (#2) structure with 26 atoms in the unit cell.[90] In this structure, two phosphate groups are connected with a "bridging" O forming $Li_4P_2O_7$ crystals. This structure, having 2 formula units per unit cell is visualized in Fig. 4 together with a hypothetical nitrogenated analog based on the same structure but with N replacing the bridging O and with the addition of an extra Li ion to maintain charge neutrality. At this time, $Li_5P_2O_6N$ remains a hypothetical idealization of a possible LiPON structure, having a stoichiometry close to the range of typical prepared films.[57]

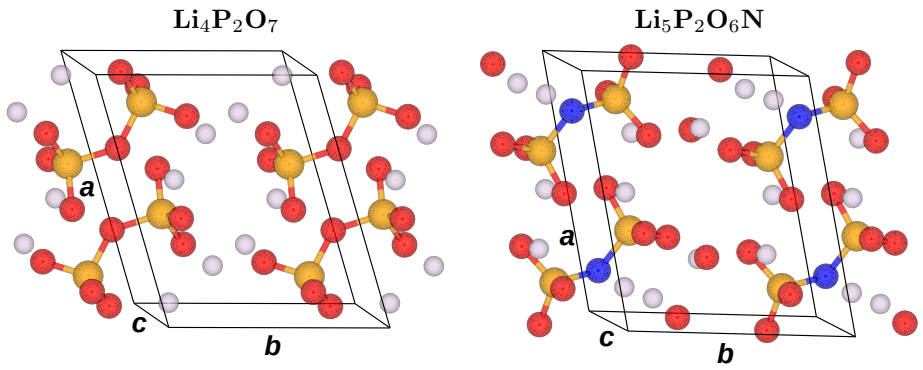

Fig. 4. Ball and stick diagrams for the $P\bar{1}$ structures of $Li_4P_2O_7$ and $Li_5P_2O_6N$ (2 formula units per unit cell) from computational results.

The thiophosphate dimer material $Li_4P_2S_7$ has been studied in its glassy form.[95] Although the crystalline form may not exist in nature, it was possible to create a metastable computer model of this structure, based on the phosphate analog as visualized in Fig. 5. While $Li_4P_2S_7$ is not known to crystallize alone, the dimer has been shown to play an important role in the the meta-stable so-called superionic ceramic material $Li_7P_3S_{11}$ which has been identified in the $P\bar{1}$ structure.[74,96] This

structure, visualized in Fig. 5 is composed of dimer and monomer substructures.[51] For completeness, the lithium phosphate analog $Li_7P_3O_{11}$ is also listed in Tables 1 and 2, even though its physical realization seems unlikely.

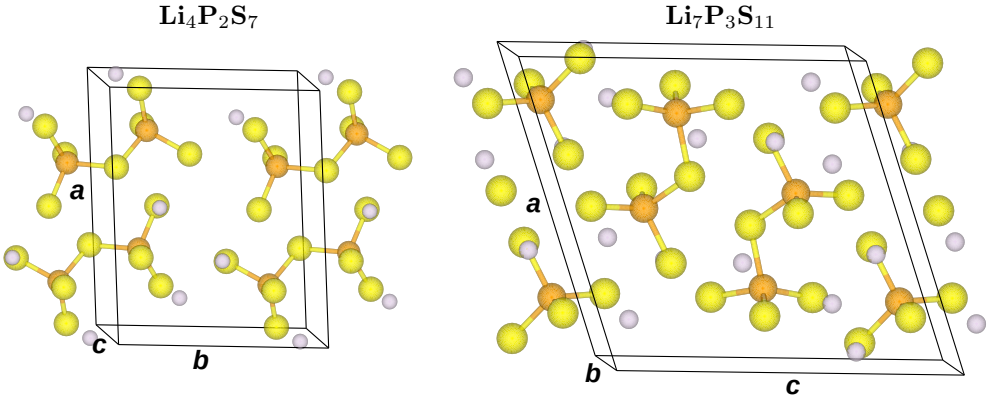

Fig. 5. Ball and stick diagrams for the $P\bar{1}$ structures of hypothetical $Li_4P_2S_7$ and the metastable superionic conductor $Li_7P_3S_{11}$ (both with 2 formula units per unit cell) from computational results.

For the Li thiophosphates, a different dimer form – $Li_4P_2S_6$ with trigonal symmetry – has been synthesized[91] and and appears to be a stable decomposition product of other Li thiophosphate electrolytes.[74] The crystal structure of $Li_4P_2S_6$ was described by Mercier *et al.*[91] as hexagonal $P6_3/mcm$ (#193) with half occupancy of the P ($4e$) sites. The electronic structure calculations of the 6 possible configurations of this unit cell find the lowest energy configuration to be described by the $P\bar{3}1m$ (#162) structure which is a subgroup of the original space group. This structure and its phosphate analog are visualized in Fig. 6. In contrast to the other materials, an interesting characteristic of the optimized $Li_4P_2S_6$ and $Li_4P_2O_6$ structures is the presence of a direct bond between two P ions,[47] indicating a more covalent configuration than the P^{+5} ionic state assumed for other phosphates and thiophosphates. While $Li_4P_2S_6$ has been reported in several studies, $Li_4P_2O_6$ is not known to exist. The heat of formation table results are consistent with the observed stability of $Li_4P_2S_6$+S compared to $Li_4P_2S_7$ and of $Li_4P_2O_7$ relative to $Li_4P_2O_6$+O.

2.2.3. *Chain-structured materials*

Crystals of $LiPO_3$ are characterized by infinite linear chains of phosphate, where in each formula unit, two O's make tetrahedral bonds with P, while the third O is involved with a bridge bond between two phosphate groups. $LiPO_3$ can be prepared from a Li_2O-P_2O_5 glass by heating[97] and its crystal structure was analyzed[92] to have the space group $P2/c$ (#13) with 100 atoms per primitive unit cell. Figure 7 shows a ball and stick model of the structure, showing the arrangement of the

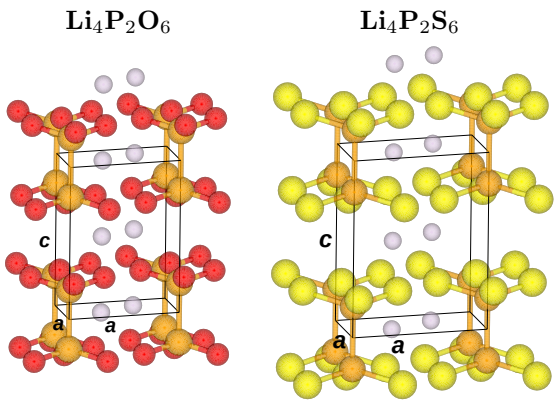

Fig. 6. Ball and stick diagrams for the $P\bar{3}1m$ structures of $Li_4P_2O_6$ and $Li_4P_2S_6$ (1 formula unit per unit cell) from computed results.

chains using lattice parameter labels consistent with Ref. [92]. A visualization of the chain structure itself is also given in the figure, showing the chain to be twisted about its axis with a periodicity of 10 phosphate groups.

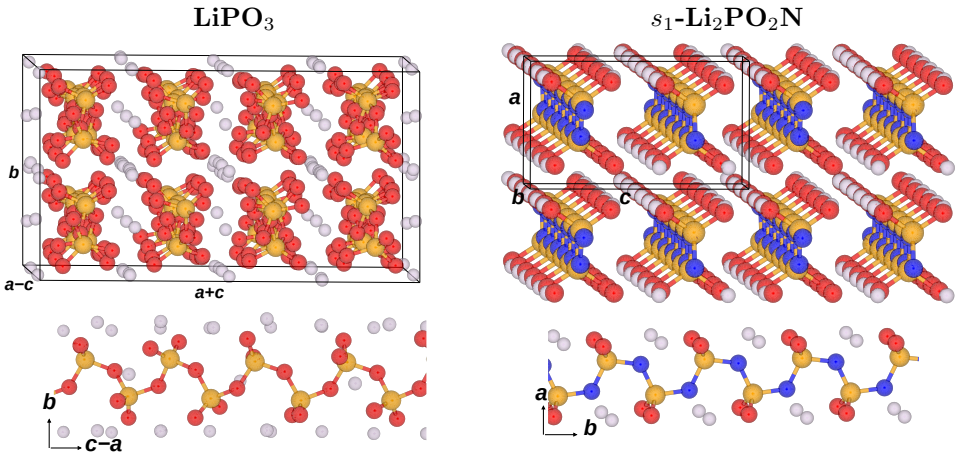

Fig. 7. Ball and stick diagrams for $LiPO_3$ in the $P2/c$ structure (20 formula units per unit cell) and $s1$-Li_2PO_2N in the $Pbcm$ structure (4 formula units per unit cell) from the calculated results. For each crystal diagram, a view of a horizontal chain axis is also provided for a single phosphate or phospho-nitride chain.

The possibility of substituting N for O in natural $LiPO_3$ was studied computationally.[49] Starting with the $P2/c$ structure of natural $LiPO_3$, the 20 bridging oxygens were substituted with nitrogens and 20 additional Li atoms were introduced into the structure to maintain charge neutrality. The relaxation results were remarkable; showing that the nitrided chain has a very stable structure with a periodicity of $(PO_2N)_2$ groups. The first optimized structure obtained from the

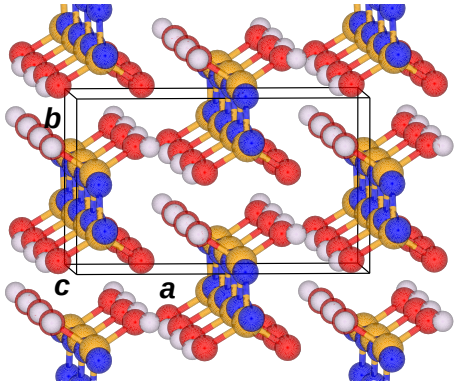

Fig. 8. Ball and stick diagram of SD-Li_2PO_2N in the $Cmc2_1$ structure (2 formula units per unit cell) from the calculated results.

simulation was called s_1-Li_2PO_2N and was found to have 24 atoms per unit cell having the space group $Pbcm$ (#57) which is visualized in Fig. 7. The most intriguing structural feature of the simulated structure of s_1-Li_2PO_2N compared to its parent $LiPO_3$ material, is the regularization of the chain structure with a planar -P-N-P-N- backbone which is also visualized in Fig. 7. In 2013, a form of Li_2PO_2N was experimentally realized by Senevirathne et. al.[52] The synthesized material, called SD-Li_2PO_2N has the $Cmnc2_1$ (#36) space group and differs from the $s1$ structure by the arrangement of the phosphate chains. Interestingly, it is structurally similar[98] to Li_2SiO_3. The solid state synthesis of SD-Li_2PO_2N used the reaction

$$Li_2O + \frac{1}{5}P_2O_5 + \frac{1}{5}P_3N_5 \rightarrow Li_2PO_2N, \tag{10}$$

which is predicted to be exothermic from the computed heats of formation given in Table 1. SD-Li_2PO_2N is visualized in Fig. 8. It is tempting to ask the question whether a similar thiophospho-nitride material could exist. Accordingly, computational studies of SD-Li_2PS_2N find a meta-stable structure and the results are recorded in Tables 1 and 2. At this time there is no evidence that this structure has be physically realized and, according to the heat of formation table, the exothermicity of the reaction analogous to Eq. (10) is smaller than the expected calculational error.

For completeness, $LiPN_2$ which was prepared and analyzed experimentally[93,99] was also studied computationally[49] and its energy and lattice results are listed in Table 1 and 2. Its $I\bar{4}2d$ (#122) structure with 2 formula units per unit cell is more complicated than the chain structures discussed in this section.

2.3. *Li ion mobilities in crystalline electrolytes*

The Li ion conductivities in many of the crystalline Li phosphates, phospho-nitrides, and thiophosphates have been studied experimentally and computationally. Some of these results are summarized in Table 3 in terms of the activation, migration, and formation energies discussed in Eqs. (6) and (7). In this table for γ-Li_3PO_4, results for different crystallographic directions are quoted to compare with single crystal experiment; in other cases, only the minimum migration energies are given.

Table 3. Calculated migration energies ($E_m^{\rm cal}$) for Li ion vacancies (vac) and interstitials (int), vacancy-interstitial formation energies ($E_f^{\rm cal}$), and corresponding the activation energies ($E_A^{\rm cal}$) for crystalline materials computed using the NEB method in idealized supercells. When available, experimental activation energies $E_A^{\rm exp}$ are also listed together with additional information including the literature reference indicated in [ ] brackets. For γ-Li_3PO_4, results for different crystallographic directions are quoted to compare with single crystal experiment; in other cases, only the minimum energies are given. All energies are given in eV.

Material	vac $E_m^{\rm cal}$	int $E_m^{\rm cal}$	$E_f^{\rm cal}$	$E_A^{\rm cal}$	$E_A^{\rm exp}$	Reference
β-Li_3PO_4	0.7	0.4	2.1	1.4		
γ-Li_3PO_4	0.7, 0.7	0.4, 0.3	1.7	1.3, 1.1	1.23, 1.14	(sngl. cryst.) [100]
$Li_{2.88}PO_{3.73}N_{0.14}$					0.97	(poly cryst.) [58]
$Li_{3.3}PO_{3.9}N_{0.17}$					0.56	(amorphous) [58]
$Li_{1.35}PO_{2.99}N_{0.13}$					0.60	(amorphous) [101]
$LiPO_3$	0.6	0.7	1.2	1.2	1.4	(poly cryst.) [97]
					0.76-1.2	(amorphous) [97]
$LiPN_2$	0.4		2.5	1.7	0.6	(poly cryst.) [99]
SD-Li_2PO_2N	0.4	0.8	2.0	1.4	0.6	(poly cryst.) [52]
γ-Li_3PS_4	0.3		0.8	0.7	0.5	(poly cryst.) [102]
β-Li_3PS_4	0.2		0.0	0.2	0.4	(nano cryst.) [103]
$Li_7P_3S_{11}$	0.2	0.5	0.0	0.2	0.1	(poly cryst.) [76]

From the results reported in Table 3, the calculated and measured activation energies for crystalline γ-Li_3PO_4 and for crystalline $LiPO_3$ are in reasonably good agreement. In both of these crystals, the activation energy for ionic conduction is dominated by a large formation energy E_f. For results on amorphous preparations of the same materials, the reported values of E_A^{exp} are much smaller and consistent with the assumption that the samples have temperature independent reservoirs of Li defect sites so that $E_A \approx E_m$. The fact $E_A^{exp} \approx E_m^{cal}$ for $LiPN_2$ and SD-Li_2PO_2N suggests that those samples also have significant temperature independent reservoirs of Li defect sites.

In contrast to the Li phosphates and phospho-nitrides, the ionic conductivities of Li thiophosphates are significantly higher, consistent with the computer modeling results which indicate that the Li thiophosphates have generally smaller migrations energies E_m^{cal}. In addition, several configurations of Li ion vacancy-interstitial pairs have been found to have negligible formation energies E_f^{cal}. Small values of E_m^{cal} and

E_f^{cal} are consistent with to the generally small activation energies for ion conduction measured for these materials.

In addition to the bulk ionic conductivity, practical electrolytes must also form stable interfaces with the electrode materials. Modeling of idealized interfaces of electrolytes with pure Li films find[53] that Li phosphate/Li interfaces are stable while Li thiophosphate/Li interfaces are not. Further modeling work is needed to investigate this issue.

3. Li oxide garnet electrolytes

Metal oxide materials have been investigated for their utility as solid electrolytes for Li ion batteries for more than 25 years. Stability against a Li metal anode, an electronic band gap with a technologically suitable magnitude (minimum of 4.5 eV), chemical stability under operating voltages and temperatures and high ionic conductivity are among the essential characteristics for battery usage. Very few materials satisfy all of these criteria simultaneously. Many potential materials are unstable against Li metal,[104–111] while others readily undergo decomposition.[112–114] Garnet structured oxides, such as $Li_5La_3M_4O_{12}$ (M=Ta,Nb)[115] have been shown to have conductivities rivaling LiPON, but only the Ta version is stable against Li and has a conductivity of $\sim 10^{-6} S/cm$. This is still a full three orders of magnitude lower than traditional liquid electrolytes.

3.1. *Two phase garnet oxides*

Recently, a new garnet oxide material, $Li_7La_3Zr_2O_{12}$ (LLZO), was shown to have a conductivity as high as $\sigma = 1.9\text{x}10^{-4}$ S/cm, while also remaining stable against Li.[116,117] Unfortunately, the synthesis of this material produced two distinct phases: a cubic one with the observed high conductivity and a tetragonal one with a much lower conductivity of $\sigma_{tetra} = 1.63\text{x}10^{-6}$ S/cm.[118] The determining factor between phases was, for many years, unknown. Thus progress toward practical usage of this material was hampered by the appearance of the unwanted tetragonal phase during synthesis.

In Fig. 9, the two phases are shown. The tetragonal phase has an ordered Li sublattice with three distinct symmetry sites, Li(1), Li(2) and Li(3), all fully filled. The cubic phase has only two distinct Li sites, but both of them are partially filled, leading to overall disorder on the Li sublattice. In 2011, Geiger *et al.*[119] noted that if the material was synthesized in Pt crucibles, *only* the tetragonal phase emerged, whereas synthesis in the more common alumina crucibles produced a mix of tetragonal and cubic phases. This lead to the hypothesis that accidental incorporation of Al must contribute to the emergence of the cubic, high conductivity form of LLZO. By intentionally incorporating Al during synthesis, Rangasamy *et al.*[120] proved the correctness of the hypothesis and established a critical Al concentration of 0.20 moles per formula unit for achieving the high conductivity cubic phase. These two

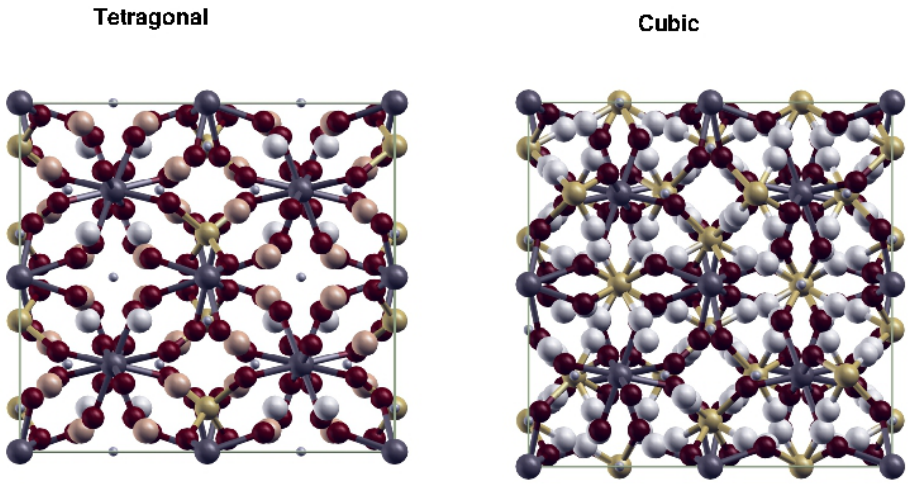

Fig. 9. Crystal structure of tetragonal (left) and cubic (right) phases of LLZO. Dark gray (large) spheres are Zr, red spheres are O, and tiny grey spheres are La. All Li positions are included, although in the cubic phase not all are occupied. The Li(1) atoms are gold, Li(2) are white, and Li(3) are pink.

results significantly clarified the experimental landscape, but simultaneously raised interesting fundamental questions: 1) By what mechanism does Al cause the structural lattice transition? and 2)Why is it accompanied by a two order-of-magnitude increase in conductivity?

3.2. *Dopant site preference*

To answer these questions, it was first necessary to determine where in the lattice Al sits. Density functional theory calculations of defect site preference show that Al strongly prefers to enter the Li sublattice and that the Li(1) site is the lowest energy position. Li(2) and Li(3) sites in the tetragonal lattice are significantly less favorable by 1.42 eV and 1.23 eV, respectively. This large energy barrier virtually guarantees that, at least at reasonably low concentrations, dopant Al will be located at Li(1) sites. Since Al has a 3^+ valency and Li has a 1^+ valency, a second defect or defects are necessary to achieve charge balance. Calculations show that the lowest energy compensating defect is a Li vacancy. In addition to the Li(1) displaced by Al, two of these vacancies are necessary to balance the system. These vacancies preferentially occupy the Li(2) or Li(3) sites with equal probability, based on defect calculations, with the formation of a Li(1) site vacancy is 0.1 eV higher in energy. The near equality of all vacancy formation energies indicates Li(1) vacancies are likely present along with those at Li(2) and Li(3) sites in Al-doped LLZO. Addition of Al^{3+} during synthesis therefore produces a Li deficient compound with one Al defect at a Li(1) site and two further Li vacancies in the Li sublattice. Note that the

Li(1) site functions as a "crossroads" for the Li ion pathways so that any immobile ion occupying this site would be expected to hinder Li ion diffusion.

The arrangement of the Al-induced vacancies is a major factor in the shape of the lattice itself,[54] but the precise distribution of vacancies was twice determined experimentally with very different results. In Fig. 10, the Li sublattice in the cubic and tetragonal cells is shown with the Wyckoff position labels of the Li(1) tetrahedral and Li(2)/Li(3) octahedral sites labeled.

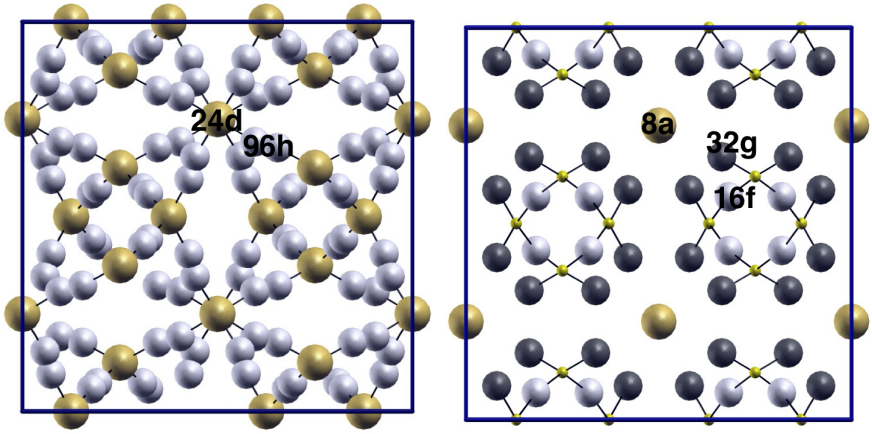

Fig. 10. The Li sublattices of cubic (left) and tetragonal (right). The Li(1) atoms are the larger gold spheres in both structures, with Li(2) in white and Li(3) in dark gray. The very small gold spheres in the tetragonal structure are tetrahedrally coordinated sites, *i.e.* Li(1) which become fully unoccupied during the cubic to tetragonal phase transition. The crystallographic site notations for each cell type the are given in black.

One determination showed Li(1) sites being nearly fully occupied, while Li(2) sites, which have three times the multiplicity, being about 1/3 occupied.[121] A second investigation found both Li(1) and Li(2) sites were each approximately half filled.[122] First principles molecular dynamics simulations found site occupancies of 0.47 and 0.46 for Li(1) and Li(2), respectively, favoring the Xie *al.* findings. Furthermore, these calculations showed that once an Li(1) site was occupied, the surrounding four Li(2) sites were always empty and that no nearest neighbor Li(2)-Li(2) pairs were simultaneously occupied. This is due to the short distances between these neighbors and the resulting strong Coulomb repulsion between two ionized Li atoms. Because of the geometry of the crystal, this puts a hard constraint on the occupation of the Li(1) sites as a function of overall Li content in the system. For an occupation x of the three Li(1) sites available per formula unit, there are $4x$ unoccupied Li(2) sites out of the twelve available per formula unit. Therefore, if Li(1) sites were nearly fully occupied as in Awaka *et al.*,[121] there would $0.94 \times 3 = 2.82$ Li located at the Li(1) site and $4 \times 2.82 = 11.28$ mandatory vacancies in the Li(2) sublattice. This leaves only 0.72 Li(2) sites available for occupation,

yielding an overall Li concentration of 3.54, far below the observed concentration of 0.65 - 0.70. As the Li concentration decreases, for instance as a function of Al doping, more Li(1) sites may be occupied, provided four nearby Li(2) vacancies are available.

3.3. *The role of dopant-induced vacancies*

In addition to elucidating the Li distribution in Al-doped LLZO, density functional calculations reveal that disorder on the Li sublattice is the driving force behind the tetragonal to cubic transition and that there is a critical number of vacancies necessary for disorder to occur. Relaxed stoichiometric LLZO (*i.e.* 7 Li per formula unit) is always tetragonal, regardless of the starting configuration of the lattice parameters. By randomly removing Li and compensating with a uniformly charged positive background to eliminate the complicating effects of Al itself (to be discussed later), it can be shown that the system will relax away from tetragonal to either cubic or orthorhombic, depending on the particular Li configuration calculated. Since in reality the Li is mobile and entropy effects are present, this indicates that random vacancies alone are sufficient to drive the system into a cubic ground state. To pinpoint the critical concentration of vacancies necessary to stabilize the cubic phase, the energy difference between a constrained tetragonal and constrained cubic cells with identical vacancy configurations were calculated. All internal coordinates along with the lattice parameters (subject only to the symmetry constraint) were calculated for 40 randomized vacancy configurations per vacancy concentration. The results are shown in Fig. 11 using both the mean and lowest energy configurations of the 40 calculations. The transition occurs when the line crosses zero and, as can be seen in the Figure, the critical concentration occurs somewhere between 0.39 and 0.43 vacancies per formula unit, in remarkable agreement with the experimentally determined number of 0.41 per formula unit.[120]

To further verify that the cubic ground state is stabilized upon creation of vacancies in the Li sublattice, Bernstein *et al.*[54] used a variable cell shape version of molecular dynamics, and added 0.25 vacancies per formula unit, a number above both the theoretically and experimentally determined critical concentration. The vacancies were inserted randomly into the ordered, tetragonal unit cell. Within 5-10 ps of simulation time, the system spontaneously converted to cubic. Thereafter, it experienced some fluctuation between cubic and tetragonal states, settling permanently into a cubic, Li-disordered ground state after 30 ps. As can be seen in Fig. 12 (top panel) the ratios a_x/a_z and a_y/a_z drop from above 1.0 to very near 1.0, indicating a cubic phase. When this drop occurs, there is a concurrent change in the distribution of the Li. The Li(1) tetrahedral sites and Li(2)/Li(3) octahedral sites have different crystallographic notations in the two different symmetry cells (cubic and tetragonal). However, it is possible to map every site in the tetragonal cell onto a corresponding site in the cubic cell (Fig. 12 bottom panel). In doing this, we can understand how the Li shifts in concert with the phase transition. There is a

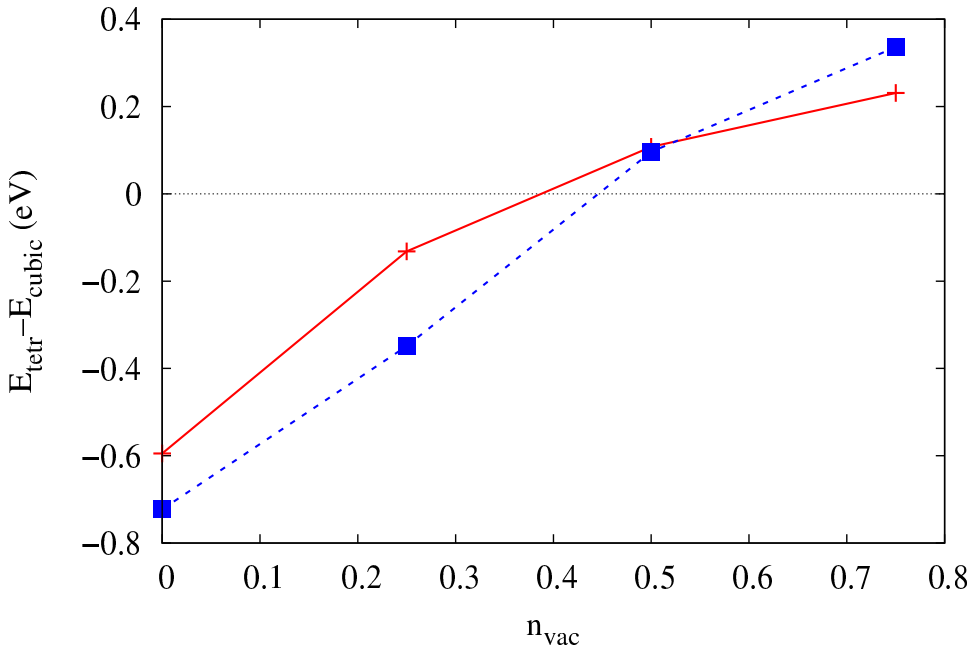

Fig. 11. Energy difference between tetragonal and cubic structures as a function of vacancy number, for minimum energy configuration (solid red line) and mean configuration energy (dashed blue line). This figure was reproduced from Ref. 54 with permission.

sharp drop in the occupancy of the 16f and 32g sites associated with the tetragonal symmetry. These are octahedrally coordinated Li(2)/Li(3) sites in the tetragonal unit cell. In the cubic cell, these correspond to Li(2) sites with the 96h symmetry label. As 96h experiences neither an increase nor decrease coincident with the phase transition, it can be assumed that the non-Li(1) site occupancy remains relatively constant. On the other hand there is also a clear dip in the originally fully occupied tetrahedral Li(1) sites with the 8a label in the tetragonal cell (Fig. 12 bottom panel). This drop is accompanied by an increase in the originally fully unoccupied 16e symmetry sites of the tetragonal cell. Again the overall occupancy of these sites when projected in the cubic cell (24d) remains constant. Therefore, the disorder can be gauged not only by the change in the lattice constants, but the sudden occupation of formally empty 16e octahedral sites in the "tetragonal" cell, which concurrently transitions to cubic.

3.4. *Fundamental mechanisms of the phase transition*

First principles calculations have also illuminated the fundamental underlying mechanism that causes the cubic state to stabilize upon vacancy creation. The link between Li distribution and lattice symmetry suggests that Li ordering, perhaps driven by Coulomb repulsion, breaks the symmetry and the lattice distorts as a

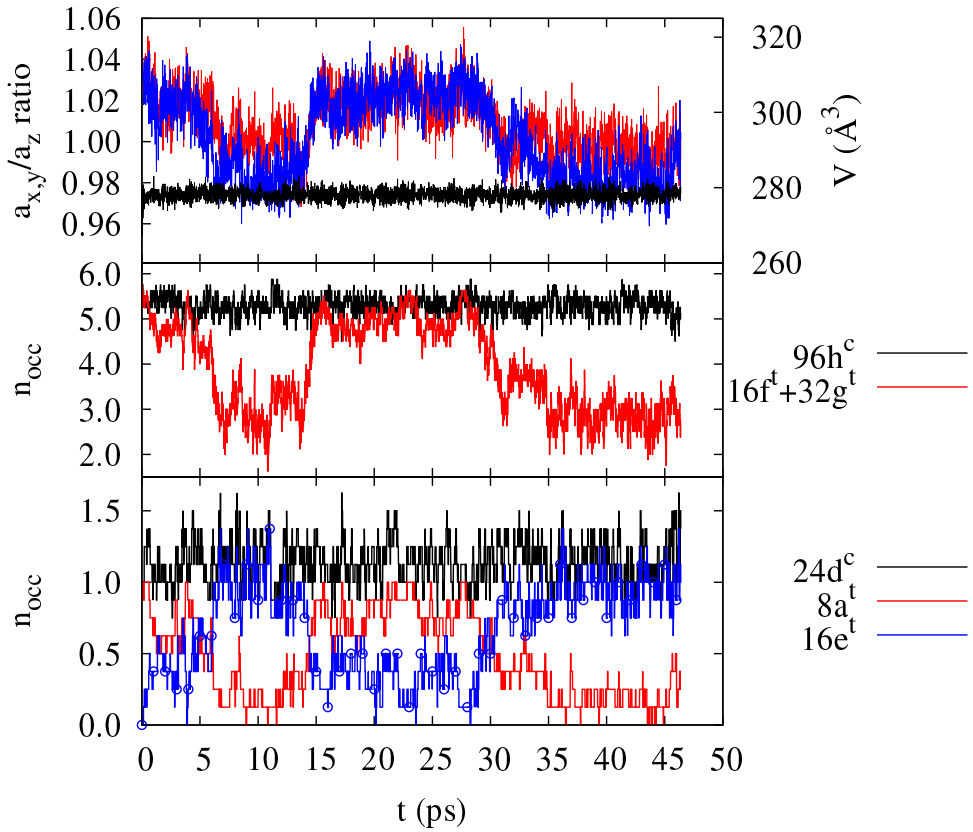

Fig. 12. Evolution over time of structural and site occupation quantities for a sample system with $n_{\mathrm{vac}} = 2$ at $T = 600$ K. Top: unit cell shape (a_x/a_z blue, a_y/a_z red) and volume (black). Middle: $96\mathrm{h}^c$ (black) and $16\mathrm{f}^t$+$32\mathrm{g}^t$ (red) lattice site occupation. Bottom: $24\mathrm{d}^c$ (black), $8\mathrm{a}^t$ (red) and $16\mathrm{e}^t$ (blue with symbols) lattice site occupations. This figure was reproduced from Ref. 54 with permission.

consequence. However, a point-charge model shows that the energy of the tetragonal distortion actually *increases* the overall energy compared to a Li-ordered cubic cell, indicating that Coulombic forces between ions are not the full story. Calculations with full Li stoichiometry clearly reproduce the energy advantage of the tetragonal over cubic phase with Li ordering, but interestingly, show that disorder even with stoichiometric Li content is favored over order if symmetry is cubic. Thus it is clear that there is an energy gain associated with the lattice distortion itself, rather than a simple response to Li order. By analyzing pair distribution functions of various ions in both cubic and tetragonal ordered cells, it is clear that the La-O distances are extremely rigid. This is perhaps not surprising since the 3^+ and 2^- formal vacancies are large and likely to interact strongly. Li ordering causes the oxygen ions to shift somewhat (preserving La-O distances) and this results in a distortion of the ZrO_6 octahedra. In the cubic cell, the Zr-O bond lengths are

2.130±.02Å and O-Zr-O bond angles are 180 °± 4.0°. The relaxation to a tetragonal cell relieves this distortion, restoring the octahedra to a uniform Zr-O bond length of 2.125 ±.005 Å and a O-Zr-O bond angle of 180°±.01°. Since the Zr-O bonds are expected to be at least partially covalent, this should produce an energy change unrelated to Coulombic forces. To quantitatively estimate the covalent bond distortion contribution to the overall energy lowering, we parametrize the calculated total energies of the ordered tetragonal cell as a function of Zr-O bond length and O-Zr-O bond angle by computing the energies for small displacements of an O atom and fitting to an harmonic approximation. Using the observed changes between cubic and tetragonal ZrO_6 octahedra, we find the energy lowering upon tetragonal distortion due to relief of ZrO_6 distortion accounts for nearly all of the energetic difference between a Li-ordered cubic and tetragonal cell, as can be seen in Figure 13. From this it can be concluded that covalent bonding is an essential component of the tetragonal distortion. This suggests a possible doping scheme for stabilizing the desired (high conductivity) phase through replacement of some (or all?) of the Zr with an element that bonds more weakly with the surrounding oxygen atoms.

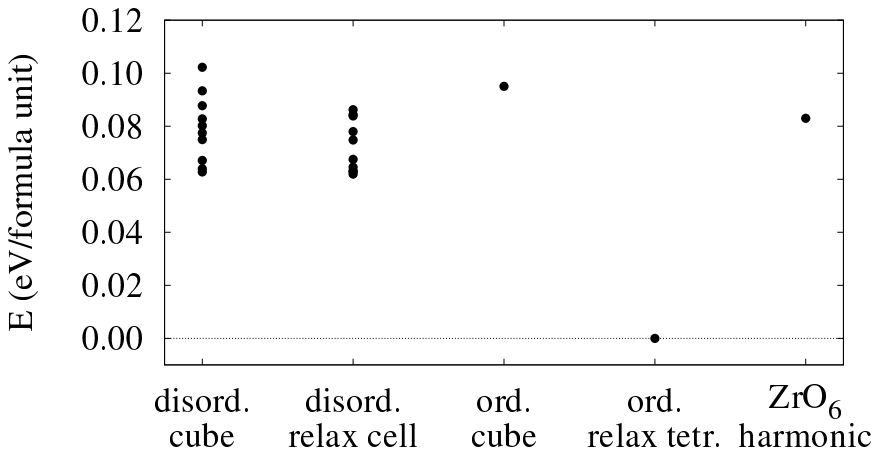

Fig. 13. Relaxed energies for 10 disordered cells with cell parameters constrained to be precisely cubic (left) and allowed to relax freely (second from left). Energies for the experimental Li ordering in a cubic cell (center) and a relaxed to tetragonal cell (second from right). The energy difference between cubic ordered and tetragonal ordered arising from bending/stretching of the covalent Zr-O bonds in the harmonic model (right). This figure was reproduced from Ref. 54 with permission.

3.5. *Li diffusion*

In addition to static DFT calculations, first principles molecular dynamics calculations were performed to gauge the Li mobility and understand its connection to Al-doping and phase change. The strict ordering of Li ions in the tetragonal phase is an obvious hindrance to movement through the lattice. Thus the very low ionic

conductivity is unsurprising. Once the Al^{3+} ions have created two vacancies on the Li sublattice, there is considerably more freedom of movement.

The mean squared displacement as a function of time, along with the best linear fit are shown in Fig. 14 for a stoichiometric cubic cell, a stoichiometric tetragonal cell, a cell doped with 0.25 Al per formula unit and a cell with the same number of vacancies as the Al-doped cell, but without the Al ion itself. For the cubic cell, the lattice constants are constrained to be equal, but otherwise unconstrained. To gauge the effect of the Al ion itself, a cell with an equal number of vacancies in the Li sublattice, but without the Al ion was created, with a uniform ("jellium") compensating positive background to balance the charge.

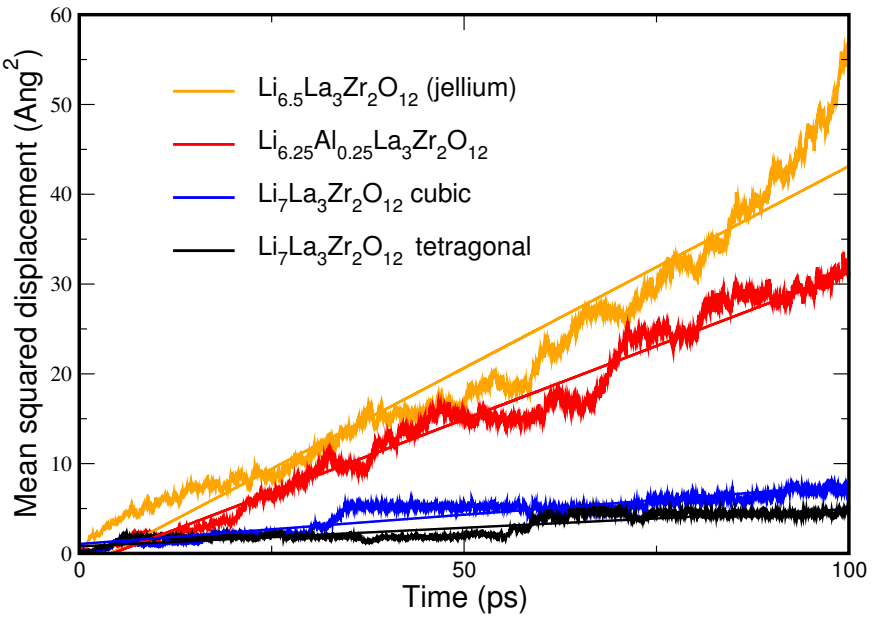

Fig. 14. The averaged mean squared displacement of Li ions in LLZO with various doping schemes at 800K. "Jellium" refers to the creation of vacancies with a uniform compensating background charge. Solid lines are the best linear fit to the data; the diffusivity is easily calculable from their slopes via Eq. 8.

As can be seen in the Figure, the actual shape of the lattice has little to no effect on the diffusivity, provided the system is stoichiometric ($Li_7La_3Zr_2O_{12}$). With 0.25 Al ions per formula unit, the cell parameters become quickly cubic (not shown) and the diffusivity is dramatically increased. With an equal number of vacancies but

without actual Al ions in the system, the diffusivity is markedly increased again. This indicates that the immobile Al ions, sitting at the crossroads site of the Li sublattice, have a "blocking" effect on the diffusivity.

3.6. *Optimizing the doping scheme*

Since there is no practical way to create vacancies without real compensating ions, alternate dopant ions that create vacancies but are physically located away from the Li sublattice are highly desirable. One possibility is Ta^{4+} which goes into the lattice at the Zr^{4+} site. Although Ta is less efficient than Al in creating vacancies (each Ta ion creates one vacancy whereas each Al creates two) it more efficiently increases the diffusivity. As can be seen in Figure 15, adding 0.25 vacancies per formula unit via Ta doping yields approximately the same diffusivity as adding 0.5 vacancies via Al doping.

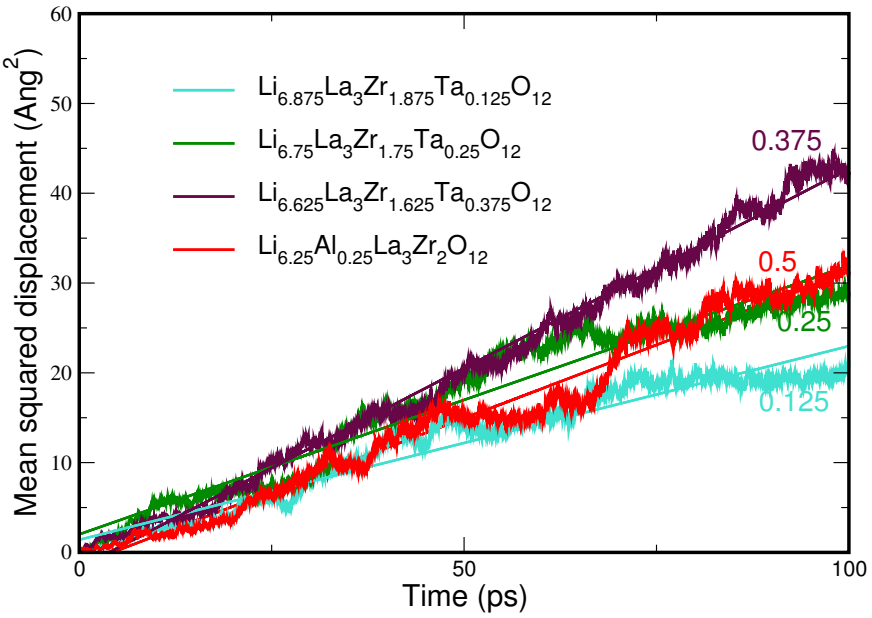

Fig. 15. The averaged mean squared displacement of Li ions in LLZO with different levels of Ta doping compared to Al doping, at 800K in each case. The solid lines are the best linear fit to the data.

Ta doping of the LLZO structure should therefore be considered the most efficient way to achieve high conductivity. Experiments have shown that Ta readily

enters the lattice at the Zr site, the resulting phase is cubic, and the conductivity is high.[123] Careful conductivity measurements to quantitatively establish its effect on conductivity remain to be done. Further computational work on this class of materials reveals that the room temperature conductivity should be extremely high, superseding that of Al-doped LLZO.[124]

4. Concluding remarks

The good agreement between first principles methodologies and the several instances of predictive power, point towards a future in which solid electrolyte materials will be greatly improved and perhaps even developed from the ground up using computational methodologies. The work in this chapter on phosphate and oxide electrolytes shows that understanding the connection between structure, electronic structure and performance is well within the realm of computational possibility. The range of crystalline forms and breadth of substitutional possibilities in the known classes of solid electrolytes alone is daunting to consider from a synthesis and testing point of view. By providing the crucial link between atomic-scale, quantum mechanical phenomena and measurable properties, simulations of solid electrolytes can be used to streamline the process and point the way towards optimized, useful materials.

Acknowledgements

The work by MDJ was funded by the Office of Naval Research (ONR) through the Naval Research Laboratory's Basic Research Program. Computational resources were provided by the DoD High Performance Computing Center. This work benefited heavily from collaborations with Noam Bernstein, Khang Hoang and Jeff Sakamoto. The work by NAWH was was supported by NSF grant DMR-1105485. Computations were performed on the Wake Forest University DEAC cluster, a centrally managed resource with support provided in part by the University. Collaborations with current and previous research assistants and associates Yaojun A. Dun, Xiao Xu, Nicholas Lepley, and Ahmad Al-Qawasmeh are gratefully acknowledged.

References

1. R. A. Huggins, *Advanced Batteries; Materials Science Aspects*. (Springer Science+Business Media, LLC, 233 Spring Street, New York, NY 10013, USA, 2009).
2. K. Takada, Progress and prospective of solid-state lithium batteries, *Acta Materialia*. **61**(3), 759–770 (Feb., 2013).
3. N. Kamaya, K. Homma, Y. Yamakawa, M. Hirayama, R. Kanno, M. Yonemura, T. Kamiyama, Y. Kato, S. Hama, K. Kawamoto, and A. Mitsui, A lithium superionic conductor, *Nature Materials*. **10**(9), 682–686, (2011).
4. S. P. Ong, Y. Mo, W. D. Richards, L. Miara, H. S. Lee, and G. Ceder, Phase stability, electrochemical stability, and ionic conductivity of the $Li_{10\pm1}MP_2X_{12}$ (M=Ge,

Si, Sn, Al or P, and X = O, S or Se) family of susperionic conductors, *Energy & Environmental Science*. **6**, 148–156, (2013).
5. M. Born and K. Huang, *Dynamical Theory of Crystal Lattices*. (Oxford at the Clarendon Press, Oxford University Press, Ely House, London.I, 1954).
6. P. Hohenberg and W. Kohn, Inhomogeneous electron gas, *Physical Review*. **136**, B864–B871, (1964).
7. W. Kohn and L. J. Sham, Self-consistent equations including exchange and correlation effects, *Physical Review*. **140**, A1133–A1138, (1965).
8. J. P. Perdew and Y. Wang, Accurate and simple analytic representation of the electron-gas correlation energy, *Phys. Rev. B*. **45**, 13244–13249, (1992).
9. J. P. Perdew, K. Burke, and M. Ernzerhof, Generalized gradient approximation made simple, *Phys. Rev. Lett.* **77**, 3865–3868, (1996). Erratum – Phys. Rev. Let. **78**, 1396 (1997).
10. U. von Barth and C. D. Gelatt, Validity of the frozen-core approximation and pseudopotential theory for cohesive energy calculations, *Phys. Rev. B*. **21**, 2222–2228, (1980).
11. J. C. Phillips and L. Kleinman, New method for calculating wave functions in crystal and molecules, *PRB*. **116**, 287–294, (1959).
12. D. R. Hamann, M. Schlüter, and C. Chiang, Norm-conserving pseudopotentials, *Phys. Rev. Lett.* **43**, 1494–1497, (1979).
13. G. P. Kerker, Non-singular atomic pseudopotentials for solid state applications, *J. Phys. C: Solid St. Phys.* **13**, L189–L194, (1980).
14. R. Car and M. Parrinello, Unified approach for molecular dynamics and density-functional theory, *Phys. Rev. Lett.* **55**, 2471–2474, (1985).
15. H. C. Andersen, Molecular dynamics simulations at constant pressure and/or temperature, *The Journal of Chemical Physics*. **72**(4), 2384, (1980).
16. M. Parrinello and A. Rahman, Polymorphic transitions in single crystals: A new molecular dynamics method, *Journal of Applied Physics*. **52**(12), 7182, (1981).
17. R. M. Wentzcovitch, Invariant molecular-dynamics approach to structural phase transitions, *Physical Review B*. **44**(5), 2358, (1991).
18. X. Gonze, First-principles responses of solids to atomic displacements and homogeneous electric fields: Implementation of a conjugate-gradient algorithm, *Physical Review B*. **55**(16), 10337, (1997).
19. X. Gonze and C. Lee, Dynamical matrices, born effective charges, dielectric permittivity tensors, and interatomic force constants from density-functional perturbation theory, *Physical Review B*. **55**(16), 10355, (1997).
20. D. Vanderbilt, Soft self-consistent pseudopotentials in a generalized eigenvalue formalism, *Phys. Rev. B*. **41**, 7892–7895, (1990). USPP code is available from the website `http://www.physics.rutgers.edu/~dhv/uspp/`.
21. P. E. Blöchl, Projector augmented-wave method, *Phys. Rev. B*. **50**, 17953–17979, (1994).
22. X. Gonze, B. Amadon, P. M. Anglade, J. M. Beuken, F. Bottin, P. Boulanger, F. Bruneval, D. Caliste, R. Caracas, M. Cote, T. Deutsch, L. Genovese, P. Ghosez, M. Giantomassi, S. Goedecker, D. R. Hamann, P. Hermet, F. Jollet, G. Jomard, S. Leroux, M. Mancini, S. Mazevet, M. J. T. Oliveira, G. Onida, Y. Pouillon, T. Rangel, G. M. Rignanese, D. Sangalli, R. Shaltaf, M. Torrent, M. J. Verstraete, G. Zerah, and J. W. Zwanziger, Abinit: First-principles approach to material and nanosystem properties, *Computer Physics Communications*. **180**(12), 2582–2615, (2009). Code is available at the website `http://www.abinit.org`.
23. P. Giannozzi, S. Baroni, N. Bonini, M. Calandra, R. Car, C. Cavazzoni, D. Ceresoli,

G. L. Chiarotti, M. Cococcioni, I. Dabo, A. D. Corso, S. de Gironcoli, S. Fabris, G. Fratesi, R. Gebauer, U. Gerstmann, C. Gougoussis, A. Kokalj, M. Lazzeri, L. Martin-Samos, N. Marzari, F. Mauri, R. Mazzarello, S. Paolini, A. Pasquarello, L. Paulatto, C. Sbraccia, S. Scandolo, G. Sclauzero, A. P. Seitsonen, A. Smogunov, P. Umari, and R. M. Wentzcovitch, Quantum espresso: a modular and open-source software project for quantum simulations of materials, *J. Phys.: Condens. Matter.* **21**(39), 394402 (19pp), (2009). Available from the website `http://www.quantum-espresso.org`.

24. N. A. W. Holzwarth, A. R. Tackett, and G. E. Matthews, A Projector Augmented Wave (PAW) code for electronic structure calculations, Part I: *atompaw* for generating atom-centered functions, *Computer Physics Communications.* **135**, 329–347, (2001). Available from the website `http://pwpaw.wfu.edu`.
25. G. Kresse and J. Furthmuller, Efficient iterative schemes for ab initio total-energy calculations using a plane-wave basis set, *Phys. Rev. B.* **54**, 111169, (1996).
26. G. Kresse and J. Furthmuller, Efficiency of ab-initio total energy calculations for metals and semiconductors using a plane-wave basis set, *Comput. Mat. Sci.* **6**(1), 15–50, (1996).
27. OpenDX – The Open Source Software Project Based on IBM's Visualization Data Explorer – is available from the web site `http://www.opendx.org`.
28. A. Kokalj, XCrySDen– an new program for displaying crystalline structures and densities, *Journal of Molecular Graphics and Modelling.* **17**, 176–179, (1999). Code available at the website `http://www.xcrysden.org`.
29. A. Kokalj, Computer graphics and graphical user interfaces as tools in simulations of matter at the atomic scale, *Computational Materials Science.* **28**, 155–168, (2003).
30. K. Momma and F. Izumi, Vesta 3 for three-dimensional visualization of crystal, volumetric, an morphology data, *Applied Crystallography.* **44**, 1272–1276, (2011). Code available from the website `http://jp-minerals.org/vesta/en/`.
31. W. M. Haynes, Ed., *CRC Handbook of Chemistry and Physics, 92th Edition.* (CRC Press, Taylor & Francis Group, 2011).
32. J. Chase, M. W., C. A. Davies, J. Downey, J. R., D. J. Frurip, R. A. McDonald, and A. N. Syverud. NIST JANAF Thermochemical Tables 1985, (1986). Available from the website `http://kinetic.nist.gov`.
33. H. Jónsson, G. Mills, and K. W. Jacobsen. Nudged elastic band method for finding minimum energy paths of transitions. In eds. B. J. Berne, G. Ciccotti, and D. F. Coker, *Classical and Quantum Dynamics in Condensed Phase Simulations*, pp. 385–404. World Scientific, Singapore, (1998).
34. G. Henkelman, B. P. Uberuaga, and H. Jónsson, A climbing image nudged elastic band method for finding saddle points and minimum energy paths, *J. Chem. Phys.* **113**, 9901–9904, (2000).
35. G. Henkelman and H. Jónsson, Improved tangent estimate in the nudged elastic band method for finding minimum energy paths and saddle points, *J. Chem. Phys.* **113**, 9978–9985, (2000).
36. N. F. Mott and R. W. Gurney, *Electronic Processes in Ionic Crystals.* (Dover Publications, Inc., New York, USA, 1964).
37. A. R. West, *Basic Solid State Chemistry.* (John Wiley & Sons, LTD, Chichester, England, 1999).
38. B. N. Mavrin, V. V. Asonov, V. V. Fomichev, A. K. Ivanov-Shitz, and V. V. Kireev, Raman scattering and interaction and interference of optical vibrations in a γ-Li_3PO_4 superionic crystal, *Journal of Experimental and Theoretical Physics.* **96**, 53–58, (2003).

39. F. Harbach and F. Fischer, Raman spectra and optical absorption edge of Li_3PO_4 single crystals, *Phys. Stat. Sol. (b).* **66**, 237–245, (1974).
40. L. Popović, B. Manoun, D. de Wall, M. K. Nieuwoudt, and J. D. Comins, Raman spectroscopic study of phase transitions in Li_3PO_4., *Journal of Raman Spectroscopy.* **34**, 77–83, (2003). Numerical values of the frequencies reported in this paper were obtained by manually digitizing the unlabeled peaks.
41. Y. A. Du and N. A. W. Holzwarth, Mechanisms of Li^+ diffusion in crystalline Li_3PO_4 electrolytes from first principles, *Phys. Rev. B.* **76**, 174302 (14 pp), (2007).
42. P. Tarte, Isomorphism and polymorphism of the compounds Li_3POi_4, Li_3AsO_4, and Li_3VO_4, *Journal of Inorganic and Nuclear Chemistry.* **29**, 915–923, (1967).
43. T. Riedener, Y. Shen, R. J. Smith, and K. L. Bray, Pressure induced phase transition and spectroscopy of Mn^{5+}- doped Li_3PO_4, *Chemical Physics Letters.* **321**, 445–451, (2000).
44. R. J. Smith, Y. Shen, and K. L. Bray, The effect of pressure on vibrational modes in li3po4, *J. Phys.: Condens. Matter.* **14**, 461–469, (2002).
45. Y. A. Du and N. A. W. Holzwarth, Effects of O vacancies and N or Si substitutions on Li^+ migration in Li_3PO_4 electrolytes from first principles, *Phys. Rev. B.* **78**, 174301, (2008).
46. Y. A. Du and N. A. W. Holzwarth, Li ion migration in Li_3PO_4 electrolytes: Effects of O vacancies and N substitutions, *ECS Transactions.* **13**, 75–82, (2008).
47. N. A. W. Holzwarth, N. D. Lepley, and Y. A. Du, Computer modeling of lithium phosphate and thiophosphate electrolyte materials, *Journal of Power Sources.* **196**, 6870–6876, (2011).
48. Y. A. Du and N. A. W. Holzwarth, First principles simulations of Li ion migration in materials related to LiPON electrolytes, *ECS Trans.* **25**(36), 27–36, (2010).
49. Y. A. Du and N. A. W. Holzwarth, First-principles study of LiPON and related solid electrolytes, *Phys. Rev. B.* **81**, 184106 (15pp), (2010).
50. N. D. Lepley and N. A. W. Holzwarth, Computer modeling of crystalline electrolytes – lithium thiophosphates and phosphates, *Transactions of the Electrochemical Society.* **35**(14), 39–51, (2011).
51. N. D. Lepley and N. A. W. Holzwarth, Computer modeling of crystalline electrolytes – lithium thiophosphates and phosphates, *Journal of the Electrochemical Society.* **159**, A538–A547, (2012).
52. K. Senevirathne, C. S. Day, M. D. Gross, A. Lachgar, and N. A. W. Holzwarth, A new crystalline LiPON electrolyte: Synthesis, properties, and electronic structure, *Solid State Ionics.* **333**, 95–101, (2013).
53. N. D. Lepley, N. A. W. Holzwarth, and Y. A. Du, Structures, Li+ mobilities, and interfacial properties of solid electrolytes Li_3PS_4 and Li_3PO_4 from first principles, *Phys. Rev. B.* **88**, 104103 (11 pp), (2013).
54. N. Bernstein, M. D. Johannes, and K. Hoang, Origin of the Structural Phase Transition in $Li_7La_3Zr_2O_{12}$, *Phys Rev Lett.* **109**(20), 205702, (2012).
55. N. J. Dudney, Thin film micro-batteries, *Interface.* **17(3)**(3), 44–48, (2008).
56. J. B. Bates, N. J. Dudney, B. Neudecker, A. Ueda, and C. D. Evans, Thin-film lithium and lithium-ion batteries, *Solid State Ionics.* **135**, 33–45, (2000).
57. X. Yu, J. B. Bates, J. G. E. Jellison, and F. X. Hart, A stable thin-film lithium electrolyte: Lithium phosphorus oxynitride, *Journal of the Electrochemical Society.* **144**, 524–532, (1997).
58. B. Wang, B. C. Chakoumakos, B. C. Sales, B. S. Kwak, and J. B. Bates, Synthesis, crystal structure, and ionic conductivity of a polycrystalline lithium phosphorus oxynitride with the γ-Li_3PO_4 structure, *Journal of Solid State Chemistry.* **115**,

313–323, (1995).
59. J. B. Bates, N. J. Dudney, D. C. Lubben, G. R. Gruzalski, B. S. Kwak, X. Yu, and R. A. Zuhr, Thin-film rechargeable lithium batteries, *Journal of Power Sources*. **54**, 58–62, (1995).
60. B. Wang, B. S. Kwak, B. C. Sales, and J. B. Bates, Ionic conductivities and structure of lithium phosphorus oxynitride glasses, *Journal of Non-Crystalline Solids*. **183**, 297–306, (1995).
61. J. B. Bates, G. R. Gruzalski, N. J. Dudney, C. F. Luck, and X. Yu, Rechargeable thin-film lithium batteries, *Solid State Ionics*. **70–71**, 619–628, (1994).
62. J. B. Bates, N. J. Dudney, G. R. Gruzalski, R. A. Zuhr, A. Choudhury, D. F. Luck, and J. D. Robertson, Fabrication and characterization of amorphous lithium electrolyte thin films and rechargeable thin-film batteries, *Journal of Power Sources*. **43–44**, 103–110, (1993).
63. J. B. Bates, N. J. Dudney, G. R. Gruzalski, R. A. Zuhr, A. Choudhury, D. F. Luck, and J. D. Robertson, Electrical properties of amorphous lithium electrolyte thin films, *Solid State Ionics*. **53–56**, 647–654, (1992).
64. A. Patil, V. Patil, D. W. Shin, J.-W. Choi, D.-S. Paik, and S.-J. Yoon, Issue and challenges facing rechargeable thin film lithium batteries, *Materials Research Bulletin*. **43**, 1913–1942, (2008).
65. N. Mascaraque, J. L. G. Fierro, A. Durán, and F. Muñoz, An interpretation for the increase of ionic conductivity by nitrogen incorporation in LiPON oxynitride glasses, *Solid State Ionics*. **233**, 73–79, (2013).
66. Y. G. Kim and H. Wadley, Plasma-assisted deposition of lithium phosphorous oxynitride films: Substrate bias effects, *Journal of Power Sources*. **187**, 591–598, (2009).
67. Y. Hamon, A. Douard, F. Sabary, C. Marcel, P. Vinatier, B. Pecquenard, and A. Levasseur, Influence of sputtering conditions on ionic conductivity of LiPON thin films, *Solid State Ionics*. **177**, 257–261, (2006).
68. H. Y. Park, S. C. Ham, Y. C. Lim, K. G. Choi, K. C. Lee, G. B. Park, S.-R. L. H. P. Kim, and S. B. Cho, Effects of sputtering pressure on the characteristics of lithium ion conductive lithium phosphorous oxynitride thin film, *J. Electroceram.* **17**, 1023–1030, (2006).
69. B. Wang, J. B. Bates, F. X. Hart, B. C. Sales, R. A. Zuhr, and J. D. Robertson, Characterization of thin-film rechargeable lithium batteries with lithium cobalt oxide cathodes, *Journal of The Electrochemical Society*. **143**(10), 3203–3213, (1996).
70. N. J. Dudney, Addition of a thin-film inorganic solid electrolite (Lipon) as a protective film in lithium batteries with a liquid electrolyte, *Journal of Power Sources*. **89**, 176–179, (2000).
71. F. Mizuno, A. Hayashi, K. Tadanaga, and M. Tatsumisago, New lithium-ion conducting crystal obtained by crystallization of Li_2S-P_2S_5 glasses, *Electrochemical and Solid-State Letters*. **8**, A603–A606, (2005).
72. F. Mizuno, A. Hayashi, K. Tadanaga, and M. Tatsumisago, New, highly ion-conductive crystals precipitated from Li_2S-P_2S_5 glasses, *Adv. Mater.* **17**, 918–921, (2005).
73. F. Mizuno, T. Ohtomo, A. Hayashi, K. Tadanaga, and M. Tatsumisago, Lithium ion conducting solid electrolytes prepared from Li_2S, elemental P and S, *Solid State Ionics*. **177**, 2753–2757, (2006).
74. H. Yamane, M. Shibata, Y. Shimane, T. Junke, Y. Seino, S. Adams, K. Minami, A. Hayashi, and M. Tatsumisago, Crystal structure of a superionic conductor $Li_7P_3S_{11}$, *Solid State Ionics*. **178**, 1163–1167, (2007).
75. A. Hayashi, Preparation and characterization of glassy materials for all-solid-state

lithium secondary batteries, *Journal of the Ceramic Society of Japan*. **115**, 110–117, (2007).
76. M. Tatsumisago and A. Hayashi, Preparation of lithium ion conducting glasses and glass-ceramics for all-solid-state batteries, *Journal of Non-Crystalline Solids*. **354**, 1411–1417, (2008).
77. K. Minami, A. Hayashi, and M. Tatsumisago, Electrical and electrochemical properties of the $70Li_2S{\cdot}(30-x)P_2S_5{\cdot}xP_2O_5$ glass-ceramic electrolytes, *Solid State Ionics*. **179**, 1282–1285, (2008).
78. A. Hayashi, K. Minami, F. Mizuno, and M. Tatsumisago, Formation of Li^+ superionic crystals from the Li_2S-P_2S_5 melt-quench glasses, *J. Mater. Sci.* **43**, 1885–1889, (2008).
79. A. Hayashi, K. Minami, and M. Tatsumisago, High lithium ion conduction of sulfide glass-based solid electrolytes and their application to all-solid-state batteries, *Journal of Non-crystalline Solids*. **355**, 1919–1923, (2009).
80. J. Trevey, J. S. Jang, Y. W. Jung, C. R. Stoldt, and S.-H. Lee, Glass-ceramic Li_2S-P_2S_5 electrolytes prepared by a single step ball billing process and their application for all-solid-state lithium-ion batteries, *Electrochemistry Communications*. **11**, 1830–1833, (2009).
81. Z. Liu, W. Fu, E. A. Payzant, X. Yu, Z. Wu, N. J. Dudney, J. Kiggans, K. Hong, A. J. Rondinone, and C. Liang, Anomalous high ionic conductivity of nanoporous $\beta-Li_3PS_4$, *Journal of the American Chemical Society*. **135**(3), 975–978, (2013).
82. W. A. Crichton, M. Mezouar, G. Monaco, and S. Falconi, Phosphorus: New *in situ* powder data from large-volume apparatus, *Powder Diffraction*. **18**, 155–158, (2003).
83. S. J. Rettig and J. Trotter, Refinement of the strucgture of orthorhombic sulfur, α-S_8, *Acta Cryst. C*. **43**, 2260–2262, (1987).
84. L. Wang, T. Maxisch, and G. Ceder, Oxidation energies of transition metal oxides within the GGA+U framework, *Phys. Rev. B*. **73**, 195107–1–195107–6, (2006).
85. T. Hahn, Ed., *International Tables for Crystallography, Volume A: Space-group symmetry, Fifth revised edition*. (Kluwer, 2002).
86. A. Belsky, M. Hellenbrandt, V. L. Karen, and P. Luksch, New developments in the Inorganic Crystal Structure Database (ICSD): accessibility in support of materials research and design, *Acta Crystallographica*. **B58**, 364–369, (2002). Available from the website `http://www.fiz-karlsruhe.de`.
87. C. Keffer, A. Mighell, F. Mauer, H. Swanson, and S. Block, The crystal structure of twinned low-temperature lithium phosphate, *Inorganic Chemistry*. **6**, 119–125, (1967).
88. K. Homma, M. Yonemura, T. Kobayashi, M. Nago, M. Hirayama, and R. Kanno, Crystal structure and phase transitions of the lithium ionic conductor Li_3PS_4, *Solid State Ionics*. **182**, 53–58, (2011).
89. O. V. Yakubovich and V. S. Urusov, Electron density distribution in lithiophosphatite Li_3PO_4: Crystallochemical features of orthophosphates with hexagonal close packing, *Crystallography Reports*. **42**, 261–268, (1997).
90. A. Daidouh, M. L. Veiga, C. Pico, and M. Martinez-Ripoll, A new polymorph of $Li_4P_2O_7$, *Acta Cryst. C*. **53**, 167–169, (1997).
91. R. Mercier, J. P. Malugani, B. Fahys, J. Douglade, and G. Robert, Synthese, structure cristalline at analyse vibrationnelle de l'hexathiohypodiphosphate de lithium $Li_4P_2S_6$, *Journal of Solid State Chemistry*. **43**, 151–162, (1982).
92. E. V. Murashova and N. N. Chudinova, Synthesis and crystal structures of lithium polyphosphates, $LiPO_3$, $Li_4H(PO_3)_5$, and $LiMn(PO_3)_3$, *Crystallography Reports*. **46**, 942–946, (2001).

93. W. Schnick and J. Lücke, On lithium phosphorus nitride. preparation and refinement of the crystal structure of $LiPN_2$, *Z. anorg. allg. Chem.* **588**, 19–25, (1990).
94. R. Mercier, J.-P. Malugani, B. Fahys, and G. Robert, Structure du tétrathiophosphate de lithium, *Acta Cryst.* **B38**, 1887–1890, (1982).
95. J. a. d. G. Schmedt and H. Eckert, High-resolution double-quantum ^{31}P NMR: A new approach to structural studies of thiophosphates, *Chem. Eur. J.* **4**, 1762–1767, (1998).
96. Y. Onodera, K. Mori, T. Otomo, A. C. Hannon, S. Kohara, K. Itoh, M. Sugiyama, and T. Fukunaga, Crystal structure of $Li_7P_3S_{11}$ studied by neutron and synchorotron X-ray powder diffraction, *J. Phys. Soc. Jpn.* **79**, 87–89, (2010). Suppl. A; Proc. 3rd Int. Conf. Physics of Solid State Ionics (ICPSSI-3).
97. B. K. Money and K. Hariharan, Lithium ion conduction in lithium metaphosphate based systems, *Applied Physics A.* **88**, 647–652, (2007).
98. K.-F. Hesse, Refinement of the crystal structure of lithium polysilicate, *Acta Cryst. B.* **33**, 901–902, (1977).
99. W. Schnick and J. Luecke, Lithium ion conductivity of $LiPN_2$ and Li_7PN_4, *Solid State Ionics.* **38**, 271–273, (1990).
100. A. K. Ivanov-Shitz, V. V. Kireev, O. K. Mel'nikov, and L. N. Demainets, Growth and ionic conductivity of γ-Li_3PO_4, *Crystallography Reports.* **46**, 864–867, (2001).
101. F. Muñoz, A. Durán, L. Pascual, L. Montagne, B. Revel, and A. C. M. Rodrigues, Increased electrical conductivity of LiPON glasses produced by ammonolysis, *Solid State Ionics.* **179**, 574–579, (2008).
102. M. Tachez, J.-P. Malugani, R. Mercier, and G. Robert, Ionic conductivity of and phase transition in lithium thiophosphate Li_3PS_4, *Solid State Ionics.* **14**, 181–185, (1984).
103. Z. Liu, W. Fu, E. A. Payzant, X. Yu, Z. Wu, N. J. Dudney, J. Kiggans, K. Hong, A. J. Rondinone, and C. Liang, Anomalous high ionic conductivity of nanoporous β-Li_3PS_4, *Journal of the American Chemical Society.* **135**(3), 975–978, (2013).
104. H. Y.-P. Hong, Crystal structure and ionic conductivity of $Li_{14}Zn(GeO_4)_4$ and other new Li^+ superionic conductors, *Materials Research Bulletin.* **13**(2), 117–124, (1978).
105. H. Aono, N. Imanaka, and G.-y. Adachi, High Li^+ conducting ceramics, *Accounts of chemical research.* **27**(9), 265–270, (1994).
106. A. D. Robertson, A. R. West, and A. G. Ritchie, Review of crystalline lithium-ion conductors suitable for high temperature battery applications, *Solid State Ionics.* **104**(1-2), 1–11, (1997).
107. A. K. Padhi, Mapping of Transition Metal Redox Energies in Phosphates with NASICON Structure by Lithium Intercalation, *J Electrochem Soc.* **144**(8), 2581, (1997).
108. Y. Inaguma, C. Liquan, M. Itoh, T. Nakamura, T. Uchida, H. Ikuta, and M. Wakihara, High ionic conductivity in lithium lanthanum titanate, *Solid State Commun.* **86**(10), 689–693, (1993).
109. H. Kawai, Lithium Ion Conductivity of A-Site Deficient Perovskite Solid Solution $La_{0.67-x}Li_{3x}TiO_3$, *J Electrochem Soc.* **141**(7), L78, (1994).
110. O. Bohnke, Mechanism of ionic conduction and electrochemical intercalation of lithium into the perovskite lanthanum lithium titanate, *Solid State Ionics.* **91**(1-2), 21–31, (1996).
111. P. Birke, Electrolytic Stability Limit and Rapid Lithium Insertion in the Fast-Ion-Conducting $Li_{0.29}La_{0.57}TiO_3$ Perovskite-Type Compound, *J Electrochem Soc.* **144** (6), L167, (1997).
112. U. v. Alpen, A. Rabenau, and G. H. Talat, Ionic conductivity in Li_3N single crystals, *Appl. Phys. Lett.* **30**(12), 621, (1977).

113. Y.-F. Y. Yao and J. T. Kummer, Ion exchange properties of and rates of ionic diffusion in beta-alumina, *Journal of Inorganic and Nuclear Chemistry.* **29**(9), 2453–2475, (1967).
114. G. Farrington, B. Dunn, and J. Briant, Li^+ and divalent ion conductivity in beta and beta" alumina, *Solid State Ionics.* **3-4**, 405–408, (1981).
115. V. Thangadurai, H. Kaack, and W. Weppner, Novel fast lithium ion conduction in garnet-type $Li_5La_3M_2O_{12}$ (M = Nb, Ta), *J. Am. Ceram. Soc.* **86**(3), 437–440, (2003).
116. R. Murugan, V. Thangadurai, and W. Weppner, Fast lithium ion conduction in garnet-type $Li_7La_3Zr_2O_{12}$, *Angew Chem Int Edit.* **46**(41), 7778–7781, (2007).
117. S. Ohta, T. Kobayashi, and T. Asaoka, High lithium ionic conductivity in the garnet-type oxide $Li_{7-x}La_3(Zr_{2-x}, Nb_x)O_{12}$ (x=0-2), *J. Power Sources.* **196**(6), 3342–3345, (2011).
118. J. Awaka, N. Kijima, H. Hayakawa, and J. Akimoto, Synthesis and structure analysis of tetragonal $Li_7La_3Zr_2O_{12}$ with the garnet-related type structure, *J. Solid State Chem.* **182**(8), 2046–2052, (2009).
119. C. A. Geiger, E. Alekseev, B. Lazic, M. Fisch, T. Armbruster, R. Langner, M. Fechtelkord, N. Kim, T. Pettke, and W. Weppner, Crystal Chemistry and Stability of $Li_7La_3Zr_2O_{12}$ Garnet: A Fast Lithium-Ion Conductor, *Inorg Chem.* **50**(3), 1089–1097, (2011).
120. E. Rangasamy, J. Wolfenstine, and J. Sakamoto, The role of Al and Li concentration on the formation of cubic garnet solid electrolyte of nominal composition i $Li_7La_3Zr_2O_{12}$, *Solid State Ionics.* **206**, 28–32 (Jan., 2012).
121. J. Awaka, A. Takashima, K. Kataoka, N. Kijima, Y. Idemoto, and J. Akimoto, Crystal Structure of Fast Lithium-ion-conducting Cubic $Li_7La_3Zr_2O_{12}$, *Chem Lett.* **40**(1), 60–62, (2011).
122. H. Xie, J. A. Alonso, Y. Li, M. T. Fernandez-Diaz, and J. B. Goodenough, Lithium Distribution in Aluminum-Free Cubic $Li_7La_3Zr_2O_{12}$, *Chem Mater.* **23**(16), 3587–3589, (2011).
123. J. L. Allen, J. Wolfenstine, E. Rangasamy, and J. Sakamoto, Effect of substitution (Ta, Al, Ga) on the conductivity of $Li_7La_3Zr_2O_{12}$, *Journal of Power Sources.* **206**, 315–319 (May, 2012).
124. L. J. Miara, S. P. Ong, Y. Mo, W. D. Richards, Y. Park, J. M. Lee, H. S. Lee, and G. Ceder, Effect of Rb and Ta Doping on the Ionic Conductivity and Stability of the Garnet $Li_{7+2x-y}(La_{3-x}Rb_x)(Zr_{2-y}Ta_y)O_{12}(0 \leq x \leq 0.375,\ 0 \leq y \leq 1)$ Superionic Conductor: A First Principles Investigation, *Chem Mater.* **25**(15), 3048–3055, (2013).